Geological Magazine

www.cambridge.org/geo

Original Article

Cite this article: Sun Z, Dong G, Santosh M, Mo X, Dong P, Wang W, and Fu B (2020) A Late Cretaceous felsic magmatic suite from the Tengchong Block, western Yunnan: integrated geochemical and isotopic investigation and implications for Sn mineralization. *Geological Magazine* **157**: 1316–1332. https://doi.org/10.1017/S0016756819001493

Received: 16 September 2019
Revised: 24 November 2019
Accepted: 3 December 2019
First published online: 24 January 2020

Keywords:
monzogranite; syenogranite; zircon Hf–O isotopes; Sr–Nd isotopes; REE tetrads; Tengchong Block

Author for correspondence:
Guochen Dong,
Email: donggc@cugb.edu.cn

A Late Cretaceous felsic magmatic suite from the Tengchong Block, western Yunnan: integrated geochemical and isotopic investigation and implications for Sn mineralization

Zhuanrong Sun[1], Guochen Dong[1], M Santosh[1,2], Xuanxue Mo[1], Pengsheng Dong[1], Weiqing Wang[1] and Bin Fu[3]

[1]School of Earth Sciences and Resources, China University of Geosciences, Beijing 100083, China; [2]Department of Earth Sciences, University of Adelaide, Adelaide SA 5005, Australia and [3]Research School of Earth Sciences, The Australian National University, Canberra ACT 2601, Australia

Abstract

The Tengchong Block within the Sanjiang Tethys belt in the southeastern part of the Tibetan plateau experienced a widespread intrusion of a felsic magmatic suite of granites in its central domain during Late Cretaceous times. Here, we investigate the Guyong and Xiaolonghe plutons from this suite in terms of their petrological, geochemical, and Sr–Nd, zircon U–Pb and Lu–Hf–O isotopic features to gain insights into the evolution of the Neo-Tethys. The Guyong pluton (76 Ma) is composed of metaluminous monzogranites, and the Xiaolonghe pluton (76 Ma) is composed of metaluminous to peraluminous medium- and fine-grained syenogranite. A systematic decrease in Eu, Ba, Sr, P and Ti concentrations; a decrease in Zr/Hf and LREE/HREE ratios; and an increase in the Rb/Ba and Ta/Nb ratios from the Guyong to Xiaolonghe plutons suggest fractional crystallization of biotite, plagioclase, K-feldspar, apatite, ilmenite and titanite. They also show the characteristics of I-type granites. The negative zircon εHf(*t*) isotopic values (−10.04 to −5.22) and high $\delta^{18}O$ values (6.69 to 8.58 ‰) and the negative whole-rock εNd(*t*) isotopic values (−9.7 to −10.1) and high initial $^{87}Sr/^{86}Sr$ ratios (0.7098–0.7099) of the Guyong monzogranite suggest that these rocks were generated by partial melting of the Precambrian basement without mantle input. The zircon εHf(*t*) isotopic values (−10.63 to −3.04) and $\delta^{18}O$ values (6.54 to 8.69 ‰) of the Xiaolonghe syenogranite are similar to the features of the Guyong monzogranite, and this similarity suggests a cogenetic nature and magma derivation from the lower crust that is composed of both metasedimentary and meta-igneous rocks. The Xiaolonghe fine-grained syenogranite shows an obvious rare earth element tetrad effect and lower Nb/Ta ratios, which indicate its productive nature with respect to ore formation. In fact, we discuss that the Sn mineralization in the region was possible due to Sn being scavenged from these rocks by exsolved hydrothermal fluids. We correlate the Late Cretaceous magmatism in the central Tengchong Block with the northward subduction of the Neo-Tethys beneath the Burma–Tengchong Block.

1. Introduction

Granitoids are the major components of upper continental crust and have been central to models of the formation, emergence, evolution and destruction of continental crust, as well as the history of supercontinents (Brown, 2013; Spencer *et al.* 2017; Roberts & Santosh, 2018; Cawood & Hawkesworth, 2019; Hawkesworth *et al.* 2019; Wang & Santosh, 2019). Granitoids are also widely used for petrogenetic modelling to understand deep crustal and crust–mantle interaction processes, including geodynamic and tectonic processes (Zhu *et al.* 2018*a*,*b*,*c*).

This study focuses on the granites from the Tengchong Block, which is located in the southwestern part of the Sanjiang Tethys tectonic domain, and corresponds to the southern extension of the Lhasa Block, which is a region that has been the focus of investigations related to the Neo-Tethyan subduction and the India–Asia collision (Fig. 1a) (Zhao *et al.* 2017*b*; Zhu *et al.* 2017*b*, 2018*b*). The large granitoids in the Tengchong Block define three N–S-trending belts from the Early Cretaceous eastern Donghe to Late Cretaceous central Guyong and Palaeogene western Binglangjiang granites (Fig. 1b) (Cao *et al.* 2016, 2018; Fang *et al.* 2018). There are also abundant synchronous tin deposits, such as the Xiaolonghe and Lailishan in the Tengchong Block (Cao *et al.* 2018). As the largest tin deposit in the Tengchong Block, the Xiaolonghe tin deposit located in the Guyong granite belt has been involved in several recent studies, which were mainly focused on the ore-forming processes and fluid evolution

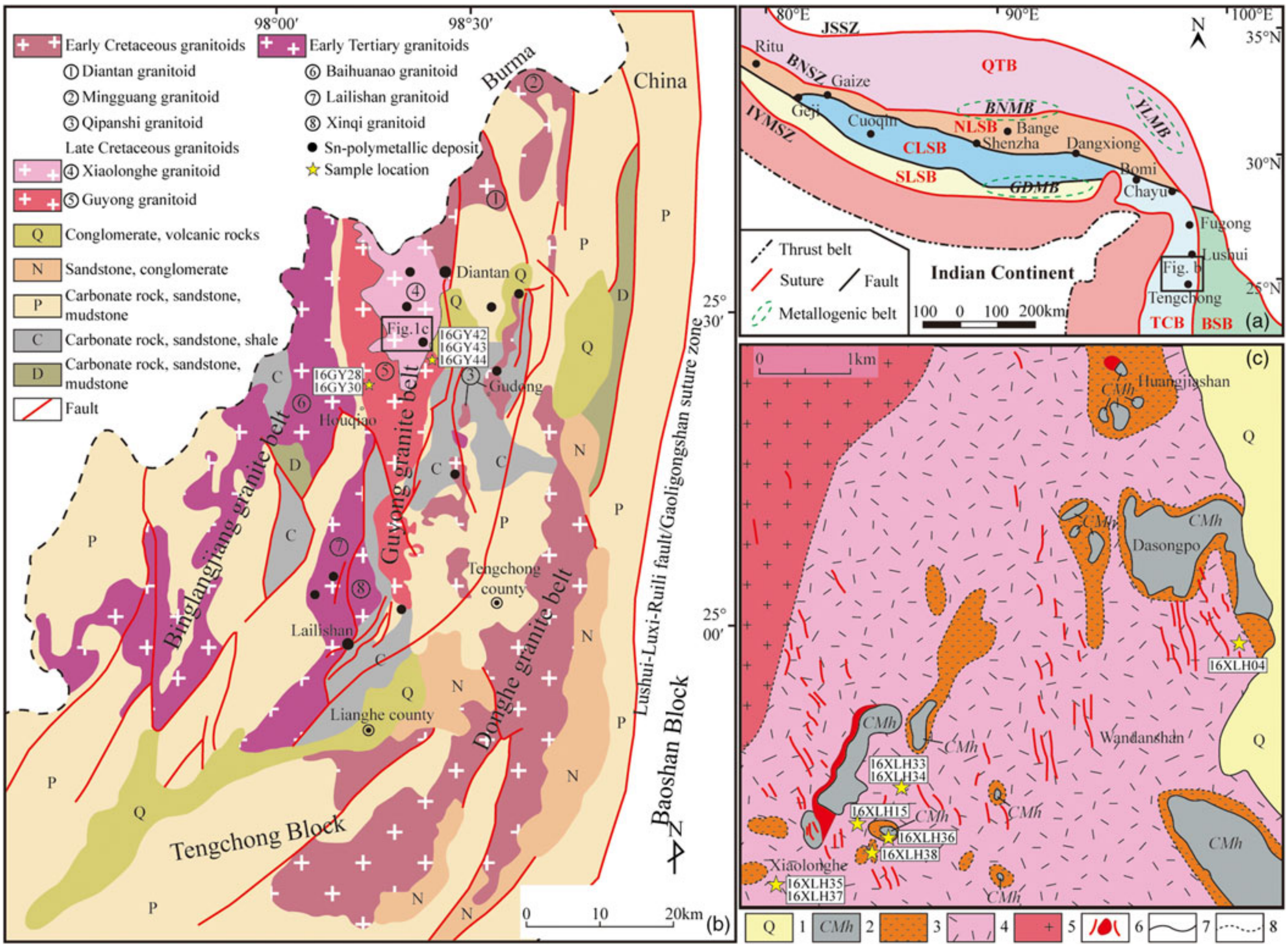

Fig. 1. (Colour online) (a) Geotectonic map of the Tengchong Block (Cao *et al.* 2014). (b) The distribution of granitoid rocks in the Tengchong Block (Chen *et al.* 2014). (c) Geological sketch of the Xiaolonghe tin deposit (Sang *et al.* 2015). Abbreviations: JSSZ – Jinsha suture zone; BNSZ – Bangong Nujiang suture zone; IYMSZ – Indus Yarlung Myitkyina suture zone; QTB – Qiangtang Block; NLSB – Northern Lhasa Block; CLSB – Central Lhasa Block; SLSB – Southern Lhasa Block; TCB – Tengchong Block; BSB – Baoshan Block; BNMB – Bangong Nujiang metallogenic belt; GDMB – Gangdese metallogenic belt; YLMB – Yulong metallogenic belt; 1 – glutenite; 2 – metasandstone and slate of Carboniferous Menghong group; 3 – Xiaolonghe fine-grained syenogranite; 4 – Xiaolonghe medium-grained syenogranite; 5 – Guyong porphyritic monzogranite; 6 – cassiterite and greisen; 7 – geological boundary; 8 – granite facies boundary.

(Chen *et al.* 2017, 2018; Cui *et al.* 2019), the geochronology of the deposit and related granites (Chen *et al.* 2014; Zhang *et al.* 2014; Cao *et al.* 2016) and the genetic link between the metallogeny and magmatism (Cao *et al.* 2016). Although the Xiaolonghe granites were considered to be related to the tin mineralization based on their geochronological and stable isotopic (C–H–O–S–Pb–He–Ar) features (Cao *et al.* 2016; Chen *et al.* 2018), and the geochronology and geochemical evolution of the Guyong porphyritic biotite granites were well studied (Xu *et al.* 2012; Xie *et al.* 2016; Zhao *et al.* 2017*b*), a systematic study of the relationship and detailed magmatic process of these different granites in the Guyong granite belt is still lacking. In addition, the question of whether the Xiaolonghe medium-grained granite or Xiaolonghe fine-grained syenogranite is related to the mineralization remains equivocal. Debate also surrounds the tectonic setting in which the Guyong and Xiaolonghe granites formed because of the complex tectonic evolution of the region (Yang *et al.* 2009; Jiang *et al.* 2012; Xu *et al.* 2012; Ma *et al.* 2013; Zhang *et al.* 2013; Chen, H. J. *et al.* 2015; Chen, X. C. *et al.* 2015; Qi *et al.* 2015; Cao *et al.* 2016; Zhao *et al.* 2017*b*).

In this study, we perform an integrated petrological, geochemical and isotopic investigation of the Guyong and Xiaolonghe intrusions, including zircon U–Pb ages, Hf–O data and whole-rock major and trace elements, and we determine Sr–Nd isotope composition. In conjunction with information from previous studies, we attempt to (1) identify the ore-forming rocks and understand the genesis of the Xiaolonghe tin deposit; (2) evaluate the petrogenesis and relationship of the Guyong and Xiaolonghe granites, as well as the relative role of mantle, lower crust and upper crust in the generation of the Guyong and Xiaolonghe granites; and (3) provide insights into the evolution of the Neo-Tethys system and the related geodynamic history of the region.

2. Geological setting

2.a. Regional geology

The Sanjiang Tethys belt located in SW China is composed of several micro-continental blocks progressively younging from east to west, such as the Baoshan and Tengchong blocks (Liu *et al.* 2009; Shi *et al.* 2015), which are separated by the Lushui–Luxi–Ruili fault (Zhu *et al.* 2015). The Tengchong Block, a northern fragment of the Sibumasu (Wang *et al.* 2014), is located in the southeastern part of the Tethyan tectonic zone (Fig. 1a), and it tectonically belongs to the suture zone of the Indian Plate and Eurasia. The subduction of the Meso-Tethys and the formation of the Neo-Tethys was induced by the northward movement of the Lhasa and west Myanmar regions during Late Triassic – Late Jurassic times (Chen *et al.* 2018). The closure of the Meso-Tethys, which formed the Bangong–Nujiang suture (Chen *et al.* 2018), occurred during Late Jurassic and Early Cretaceous times, and the closure of the Neo-Tethys occurred after Late Cretaceous times along the Indus Yarlung Myitkyina suture zone (Xu *et al.* 2012; Shi *et al.* 2015; Chen *et al.* 2018; Zhu *et al.* 2017*b*; Fang *et al.* 2018). The timing of the initial collision of the Indo-Asian continents is still uncertain and ranges from 65 Ma to 34 Ma (Chen *et al.* 2018). The successive subduction of the Meso- and Neo-Tethyan oceans resulted in a series of magmatic activities (Fig. 1b) in the Tengchong Block (Fang *et al.* 2018).

The northward subduction of the Neo-Tethyan oceanic crust beneath the Eurasian continental crust and subsequent collision between the Indian and Eurasian plates resulted in large-scale Mesozoic–Cenozoic magmatism and related mineralization, termed the Tethyan metallogenic belt (Cao *et al.* 2014; Chen *et al.* 2018; Fang *et al.* 2018). The Sanjiang Tethys tectonic domain defines the junction between Eurasia, the South China Block, India and Sunda. In addition, it is located in the southeastern Tethys tectonic domains (Fig. 1a) and is composed of several continental blocks (Liu *et al.* 2009). Granites and related ore deposits are widespread in the Sanjiang Tethys tectonic domains and form part of the Tethyan metallogenic domain. As the northernmost extension of the world-class SE Asian tin belt and the most important tin belt of the Sanjiang Tethyan Metallogenic Domain, the Tengchong–Lianghe tin belt hosts abundant granites and spatio-temporally related tin deposits (Fig. 1b; Cao *et al.* 2014; Chen, X. C. *et al.* 2015).

Magmatism in the Tengchong Block can be divided into three stages as follows: (1) The Early Cretaceous Donghe granite belt in the eastern Tengchong Block. These granites are mostly S-type granites with ages between 131 and 114 Ma, and they are enriched in large ion lithophile elements (LILEs) and depleted in high field strength elements (HFSEs) (Deng *et al.* 2014; Xie *et al.*2016). The zircon εHf(t) isotopic values of these granites reveal the increasing contributions of mantle or juvenile crustal components, and they were induced by subduction of the Meso-Tethys and collision between the Tengchong and Baoshan blocks in the eastern Tengchong Block (Qi *et al.* 2015; Xie *et al.* 2016). (2) The Late Cretaceous Guyong granite belt in the middle Tengchong Block. These granites are mainly S-type and A-type granites with ages between 76 and 65 Ma, and they have negative zircon εHf(t) isotopic values (Xie *et al.*2016) and variable whole-rock εNd(t) isotopic values between −12 and 0.5 (Jiang *et al.* 2012; Xu *et al.* 2012; Ma *et al.* 2013; Deng *et al.* 2014). (3) The Palaeogene Binglangjiang granite belt in the western Tengchong Block. These granites have ages ranging from 66 to 49 Ma, and they are mainly I-type granites with zircon εHf(t) isotopic values between −4 and +6 and S-type granites with zircon εHf(t) isotopic values between −12 and −2 (Xu *et al.* 2012; Deng *et al.* 2014; Qi *et al.* 2015; Xie *et al.* 2016; Sun *et al.* 2017). Minor Cambrian–Ordovician granites are located on either side of the Gaoligongshan zone (Cao *et al.* 2016) and the Triassic – Early Jurassic granites occur between Tengchong and Lianghe County (Zhu *et al.* 2018*c*) with ages of 520–440 Ma and 250–190 Ma, respectively (Cao *et al.* 2017*b*). In addition, there are also minor basaltic and basaltic–andesitic volcanic rocks in the Tengchong Block (Yang *et al.* 2017) with ages of 5.5–4.0 Ma, 3.9–0.9 Ma and 0.8–0.01 Ma (Zhao *et al.* 2016*a*).

The metamorphic basement of the Tengchong Block is composed of the Palaeo-Neoproterozoic Gaoligongshan Group, which is mainly distributed in the eastern and western parts of the Tengchong Block (Yang *et al.* 2017). The lower segment of the Gaoligongshan Group experienced widespread migmatization and is mainly composed of gneiss, granulite and amphibole. In contrast, the upper segment of the Gaoligongshan Group is mainly composed of schists and granulites in the absence of amphibolites, with weak migmatization compared with the lower segment (Yunnan BGMR, 1990). The zircon U–Pb ages of the paragneiss and orthogneiss from this group are 1053–635 and 490–470 Ma, respectively (Song *et al.* 2010). The basement is covered by an upper Palaeozoic – Mesozoic formation, and lower Palaeozoic sediments are absent in the Tengchong Block (Zhao *et al.* 2016*b*). The sediments in the Tengchong Block are composed of carbonate and clastic rocks from the upper Palaeozoic to lower Mesozoic. The Carboniferous, Permian and Triassic formations are composed of marbles, dolomites, limestones, quartz sandstone and siltstones. The Devonian strata are dominated by siltstones, marbles and limestones. Jurassic and Cretaceous sediments are absent (Cao *et al.* 2017*b*).

2.b. Deposit geology

As the largest tin deposit in the Tengchong–Lianghe tin belt, the Xiaolonghe tin deposit hosts more than 65,000 tonnes of tin (Liu *et al.* 2005) and is composed of four orebodies: the Xiaolonghe, Wandanshan, Dasongpo and Huangjiashan. Abundant granitoids exist in the Xiaolonghe tin ore district, including the Guyong coarse- to medium-grained porphyritic monzogranite (GPM), the Xiaolonghe medium-grained syenogranite (XMS) and the Xiaolonghe fine-grained syenogranite (XFS), which are intrusions in the Menghong Formation (Fig. 1c). Following regional metamorphism and hydrothermal alteration, the Menghong Formation within the ore field is mainly composed of hornfels with minor marbles and quartzite (Cao *et al.* 2016).

The orebodies from the Xiaolonghe tin deposit mainly occur at the top and sides of the XMS and XFS and at the inner contact zone between the syenogranite (XMS and XFS) and the Menghong Formation (Fig. 1c; Cao *et al.* 2016; Chen *et al.* 2018). These orebodies are nearly N–S distributed, which is controlled by the N–S-trending faults. Greisen vein-type mineralization mainly occurs in the deposit, which is mainly manifested as greisen veins with abundant quartz, muscovite and cassiterite, and as topaz and fluorite within the XMS and XFS (Chen *et al.* 2014, 2018; Cao *et al.* 2016). The hydrothermal alteration of the Xiaolonghe tin deposit is diverse and mainly includes greisenization, pyritization, silicification and carbonatization, and tin mineralization is mainly associated with greisenization (Cao *et al.* 2016; Chen *et al.* 2018; Cui *et al.* 2019).

2.c. Petrography and sampling

The Guyong granite belt in the central Tengchong Block is a long and narrow wedge-shaped region that is relatively wide in the north and narrow in the south. Our study area is located in the relatively wide northern part of the Guyong granite belt (Fig. 1b). The GPM, XMS and XFS compose the major intrusions in this area (Fig. 1c). Both the Guyong intrusion (GPM) and the Xiaolonghe intrusions (XMS and XFS) show direct contact with the Menghong Formation (Chen, H. J. *et al.* 2015) (Fig. 1c). The GPM in the study area is the dominant rock type, which occupies 70 % of the batholith and shows a gradational contact with the XMS (Fig. 1b). The XFS is

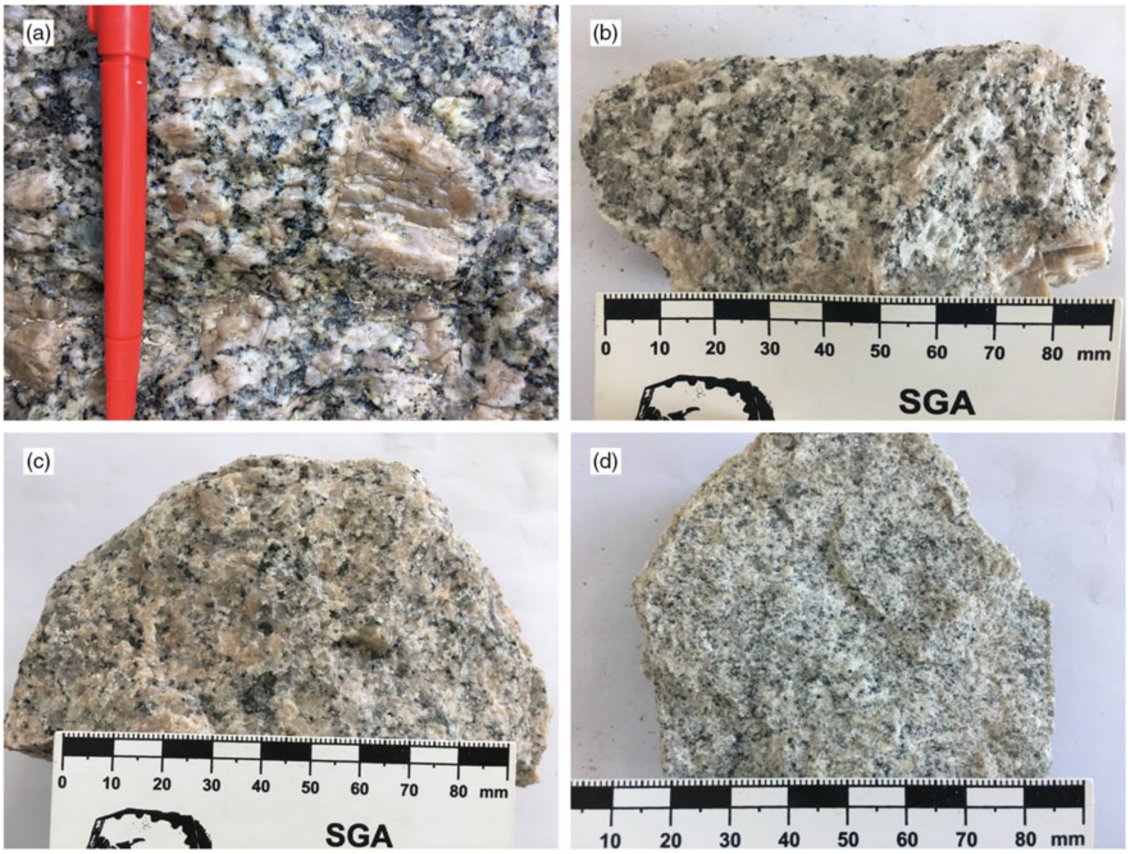

Fig. 2. (Colour online) Field photographs and hand specimens of the Guyong and Xiaolonghe plutons showing mineral composition and texture of (a, b) the Guyong porphyritic biotite monzogranite; (c) the Xiaolonghe medium-grained biotite syenogranite; and (d) the Xiaolonghe fine-grained syenogranite.

distributed in limited areas and surrounded by the XMS, and the contact between them is gradational (Fig. 1c). In this study, we collected five representative GPM samples, six XMS samples and two XFS samples. The locations of these samples are shown in Figure 1b. The GPM samples were collected across the central part of the Guyong pluton, two of which were near the western border, and the other three were near the eastern border of the Guyong pluton. One XMS sample was collected in the Dasongpo area, and the rest of the XMS samples were collected in the Xiaolonghe area. All of the XFS samples were collected in the Xiaolonghe area (Fig. 1c). Most of those samples are fresh and some are slightly altered.

The GPM is porphyritic with 15–25 vol. % phenocrysts. The phenocrysts are dominated by white plagioclase and stumpy K-feldspar (mainly orthoclase with minor perthite and microcline) with sizes up to 4.5 × 4.5 cm (Fig. 2a, b). The matrix is composed of plagioclase (~30 vol. %), K-feldspar (~35 vol. %), quartz (~25 vol. %), biotite (~8 vol. %) and minor amphiboles (Fig. 3a, b, c). The accessory minerals are represented by zircon, titanite, needle-like apatite, monazite, allanite and magnetite. Titanite exhibits typical rhombic and tabular shapes (Fig. 3b). A poikilitic texture is common in monzogranite, with biotite, titanite and quartz occurring within K-feldspar (Fig. 3d). The monzogranite exhibits slight sericitization, chloritization, argillic alteration and muscovitization, showing replacement of biotite by chlorite or muscovite and plagioclase by sericite or kaolinite.

The XMS is composed of K-feldspar (mainly orthoclase and microcline; ~35 vol. %), plagioclase (~30 vol. %), quartz (~30 vol. %) and biotite (~3 vol. %) (Figs 2c, 3e). The accessory minerals are zircon, needle-like apatite, monazite, allanite and magnetite, the contents of which are markedly less than those of the GPM. Biotite is partly replaced by muscovite, sericite and chlorite, whereas plagioclase is altered to kaolinite and sericite (Fig. 3f). Compared to the XMS, the XFS shows similar mineral assemblages with more quartz content (~35 vol. %) and less biotite content (Figs 2d, 3g). Some biotite was altered to muscovite, and the plagioclase core was replaced by muscovite (Fig. 3h).

3. Analytical methods

Preparation of sample powders for whole-rock major and trace elemental analysis, as well as for whole-rock Sr–Nd isotopic analysis, were performed at the XinHang Surveying and Mapping Institute of Hebei Province in China. Prior to crushing, fresh samples of the rocks were chipped and cleaned in 5 % HCl solution. These were then ultrasonically washed in Milli-Q water and dried in a clean environment. The dried rocks were crushed into powder (200 mesh) using an agate mill. Zircon grains for U–Pb and Hf–O isotopic studies were also separated at this Institute by conventional heavy liquid and magnetic techniques. After extraction, the samples were carefully selected after being examined under a binocular microscope. Approximately 150 representative zircon grains for each sample were mounted in epoxy resin discs that were polished and cleaned. All zircon grains were photographed under transmitted and reflected light, and then images were obtained by the cathodoluminescence (CL) technique using a JEOL JXA-8900RL microprobe before the U–Pb isotope analyses. The photomicrographs and CL images of the zircons were taken to locate the analytical spots.

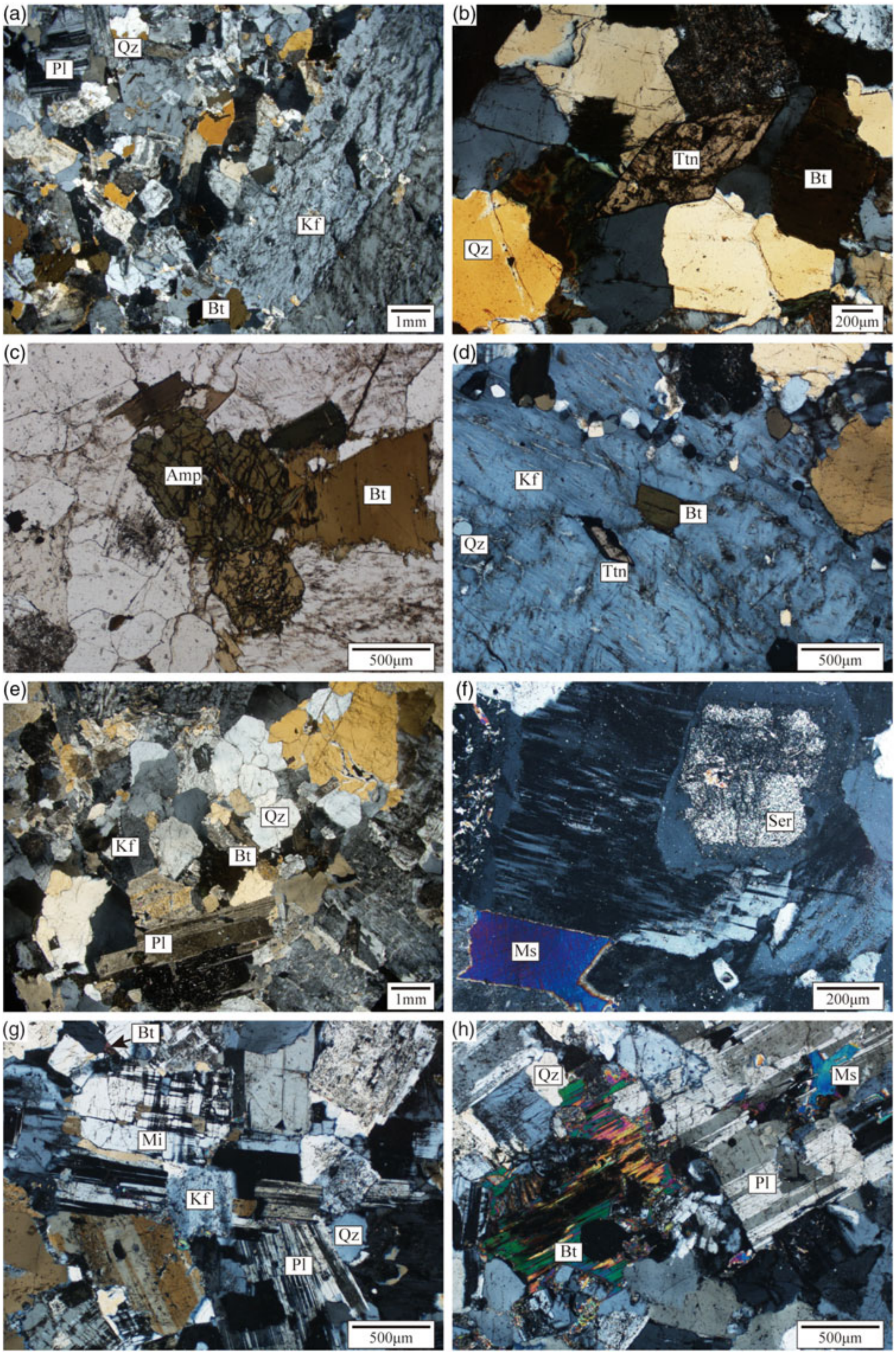

Fig. 3. (Colour online) Photomicrographs under cross-polarized light showing mineral composition and texture of (a) the Guyong porphyritic biotite monzogranite showing porphyritic texture with K-feldspar phenocryst; (b) the rhombic titanite and (c) amphibole in the monzogranite; (d) monzogranite showing poikilitic texture with biotite, titanite and quartz incorporated by K-feldspar; (e) the Xiaolonghe medium-grained syenogranite; (f) muscovite formed by the alteration of biotite and sericite from the alteration of plagioclase in the medium-grained syenogranite; (g) the Xiaolonghe fine-grained syenogranite; (h) biotite partly replaced by muscovite in the fine-grained syenogranite. Abbreviations: Qz – quartz; Pl – plagioclase; Kf – K-feldspar; Bt – biotite; Ttn – titanite; Amp – amphibole; Ser – sericite; Ms – muscovite; Mi – microcline.

3.a. Whole-rock major and trace elements

The analyses of the major elemental compositions were carried out at the State Key Laboratory of Geological Processes and Mineral Resources, China University of Geosciences, Beijing. After adding 1:5 lithium metaborate, the samples were melted at 1000 °C in a muffle furnace for 15 minutes and subsequently cooled. They were extracted with 3 % HNO_3 and diluted 2000 times to a constant volume. The major oxides were analysed by X-ray fluorescence (XRF) spectrometry (SHIMADZU XRF-1800), and the analytical precision and accuracy were better than 5 %. The analytical procedures followed those described by Cao *et al.* (2017*a*). Trace elements were analysed using an Agilent 7700e ICP-MS at the Wuhan Sample Solution Analytical Technology Co., Ltd. The analytical procedures are the same as those described by Liu *et al.* (2018). An international standard was also analysed for every ten samples, and one blank sample was analysed for all samples.

3.b. Zircon U–Pb ages and Hf–O isotope analysis

Zircon U–Pb geochronology was performed using laser ablation inductively coupled plasma mass spectrometry (LA-ICP-MS) at

https://doi.org/10.1017/S0016756819001493 Published online by Cambridge University Press

the State Key Laboratory of Geological Processes and Mineral Resources, China University of Geosciences, Beijing. The analytical methods are the same as those described by Cao *et al.* (2017*b*). The beam diameter was 35 µm with a laser frequency of 8 Hz. Zircon standard 91500 was used as the external standard and run twice for every five analytical sites, while the silicate glass standard NIST610 was used to optimise the instrument. Common Pb was corrected by the method of Andersen (2002). The off-line raw data selection, integration of background and analyte signals, and time-drift correction and quantitative calibration were conducted using ICP-MS DataCal (Liu *et al.* 2010). Age calculations and Concordia plots were carried out using Isoplot (version 4.0) (Ludwig, 2003).

In situ zircon Lu–Hf isotopic analyses were conducted using a Neptune multi-collector ICP-MS equipped with a 193 nm laser at the Tianjin Institute of Geology and Mineral Resources. During Hf isotopic analyses, a laser frequency of 10 Hz was used, and the spot size was 50 µm. Every eight-sample analysis was followed by two analyses of zircon standard GJ-1. Raw count rates for ^{172}Yb, ^{173}Yb, ^{175}Lu, ^{176}(Hf + Yb + Lu), ^{177}Hf, ^{178}Hf, ^{179}Hf, ^{180}Hf and ^{182}W were collected, and the isobaric interference corrections for ^{176}Lu and ^{176}Yb on ^{176}Hf were determined precisely. The detailed analytical technique is similar to that of Cao *et al.* (2017*a*). The zircon standard GJ-1 yielded a ^{176}Hf/^{177}Hf ratio of 0.281986 ± 0.000021 (2r, N = 88) during the data acquisition, which is consistent with the recommended ^{176}Hf/^{177}Hf ratio of 0.282015 ± 19 (Elhlou *et al.* 2006).

Zircon oxygen isotopes (^{18}O/^{16}O) were analysed by SHRIMP II and SHRIMP SI (Stable Isotope) ion microprobes at the Research School of Earth Sciences, The Australian National University, Canberra. The details of the analytical method are similar to those described by Fu *et al.* (2015).

3.c. Whole-rock Sr–Nd isotopes

The Sr–Nd isotopes were analysed at the State Key Laboratory of Geological Processes and Mineral Resources, School of Earth Sciences and Mineral Resources, China University of Geosciences, Beijing. The sample powder (50–100 mg) was dissolved with HF–HNO_3–HCl completely. After purification by resin and HCl, the Sr and Nd samples were evaporated, and their medium was changed by using 0.1 ml HNO_3. Then, they were dried again and dissolved in 3% HNO_3 as preparation for isotope analysis on the MC-ICP-MS. The Sr and Nd isotopic ratios were corrected by ^{86}Sr/^{88}Sr = 0.1194 and ^{146}Nd/^{144}Nd = 0.7219, respectively. The geological standards of BCR-2 for ^{87}Sr/^{86}Sr and ^{143}Nd/^{144}Nd were 0.705029 ± 9 (2σ) and 0.512616 ± 11 (2σ) for this study, respectively. The reference standard of SRM987 for the Sr isotope shows ^{87}Sr/^{86}Sr = 0.710274 ± 21 (2σ, N = 61) and the Alfa Nd (an ultrapure single elemental standard solution from the Alfa Aesar A Johnson Mattey Company of the USA) for the Nd isotope shows Alfa Nd = 0.512425 ± 21.

4. Results

4.a. Zircon U–Pb ages

Three samples (16GY30, 16XLH04 and 16XLH36) from the GPM, XMS and XFS were used for LA-ICP-MS zircon U–Pb dating, and the analytical data are provided in online Supplementary Material Table S1. Most of the zircon grains are colourless and transparent. They are euhedral to subhedral and 50–300 µm in length and 1:1 to 3:1 in aspect ratio. Concordia plots (Fig. 4a, b, c) and cathodoluminescence images (Fig. 4d) of representative zircons display obvious oscillatory zoning, which is a typical feature of magmatic origins. Thus, the U–Pb age is interpreted to represent the emplacement age of those granites.

Sample 16GY30 of the GPM was collected from the western part of the Guyong pluton. Twenty-three analyses yielded a weighted mean ^{206}Pb–^{238}U age of 75.9 ± 0.3 Ma (MSWD = 1.1) (Fig. 4a). One inherited zircon grain yielded a ^{206}Pb–^{238}U age of 929 Ma (Fig. 4d) and is considered to be derived from the protolith of the source materials. Sample 16XLH04 of the XMS was collected from the Xiaolonghe ore block. Twenty-four zircon grains from this rock yielded a weighted mean ^{206}Pb–^{238}U age of 75.6 ± 0.5 Ma (MSWD = 0.4) (Fig. 4c). Sample 16XLH36 of the XFS was collected from the Xiaolonghe ore block. Twenty-four zircon grains from this rock yielded a weighted mean ^{206}Pb–^{238}U age of 75.7 ± 0.3 Ma (MSWD = 0.8) (Fig. 4b). All ages above are identical within error limits.

4.b. Zircon Hf–O isotopes

In situ zircon Hf–O isotopic analysis was conducted on the same three samples (16GY30, 16XLH04 and 16XLH36) from which zircon U–Pb ages were gathered, and on the same spots on the grains (online Supplementary Material Table S2). The zircon εHf(*t*) isotopic values and two-stage model ages were calculated based on the emplacement age. Most of the ^{176}Lu/^{177}Hf ratios of the zircons are less than 0.003, which excludes any major radioactive Hf accumulation. The zircon εHf(*t*) values of samples 16GY30, 16XLH04 and 16XLH36 are −10.04 to −5.22, −10.63 to −3.48, and −9.53 to −3.04, with average values of −7.26, −6.39 and −6.86, and correspond to two-stage model ages of 1478 to 1784 Ma, 1364 to 1820 Ma, and 1339 to 1750 Ma, respectively. The zircon δ^{18}O values for the three samples 16GY30, 16XLH04 and 16XLH36 are 6.69 to 8.58 ‰, 6.54 to 8.69 ‰, and 6.60 to 8.02 ‰, with average values of 7.46, 7.65 and 7.24, respectively.

4.c. Major and trace elemental compositions

All GPM, XMS and XFS samples plot in the field of subalkalic rocks in the TAS diagram (Fig. 5a). The GPM has a limited SiO_2 content ranging from 71.34 to 73.29 wt %, and the XMS has a narrow but higher SiO_2 content ranging from 73.65 to 76.40 wt % (online Supplementary Material Table S3). The XFS has the highest SiO_2 content ranging from 76.35 to 77.33 wt %, which all belong to the field of granite (Fig. 5a). In the Q′-ANOR classification diagram, the GPM is classified as monzogranite, and the XMS and XFS belong to the field of syenogranite (Fig. 5b). The GPM is calc-alkaline and metaluminous (A/CNK = 0.95–0.98, 0.97 on average), the XMS is calc-alkaline to alkali-calcic and ranges from metaluminous to weakly peraluminous (A/CNK = 0.97–1.02, 0.99 on average), and the XFS shows a calc-alkaline affinity with weakly peraluminous features (A/CNK = 1.03–1.07, 1.05 on average) (Fig. 5c, d). The K_2O/Na_2O ratios of the GPM, XMS and XFS are 1.28–1.69, 1.54–1.75 and 1.12–1.16, and the total alkali contents (ALK = $K_2O + Na_2O$) are 7.87–8.48, 7.86–9.04 and 7.72–8.23 wt %, respectively. The XFS has a lower K_2O content (4.14–4.34 wt %) compared to the GPM (4.41–5.33 wt %) and the XMS (4.91–5.66 wt %), largely because of alteration. The differentiation index values for the GPM, XMS and XFS are 86.05–87.75 (86.85 on average), 91.06–94.35 (92.92 on average) and 93.58–95.04 (94.31 on average), respectively. The major contents (MgO, $Fe_2O_3^T$, P_2O_5 and TiO_2) clearly decrease with the increase in SiO_2 (Fig. 6) from the GPM to the XMS and XFS.

The GPM, XMS and XFS have total rare earth element (ΣREE) contents of 268.74–309.00 ppm (average 296.23 ppm),

https://doi.org/10.1017/S0016756819001493 Published online by Cambridge University Press

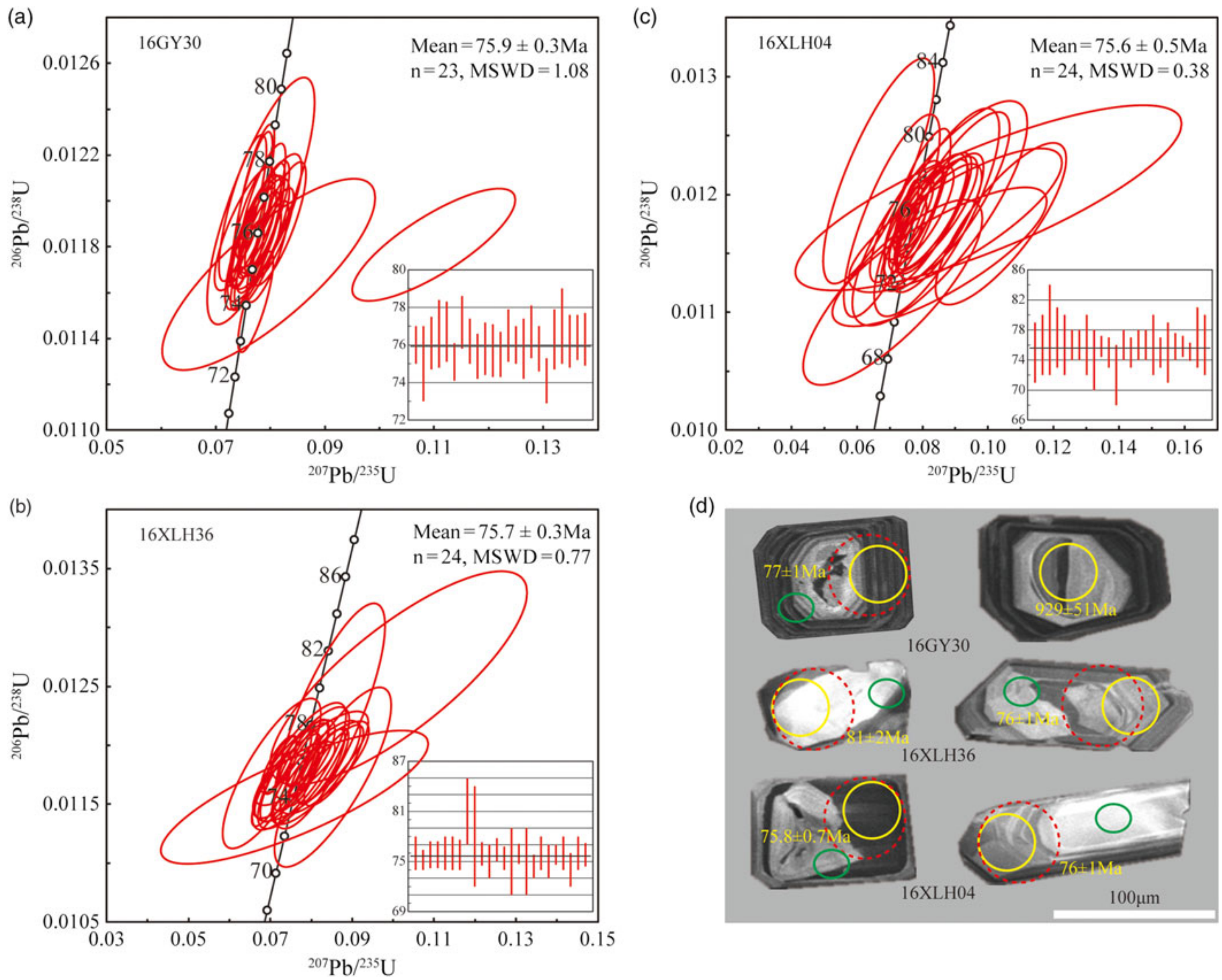

Fig. 4. (Colour online) (a–c) Zircon U–Pb Concordia diagrams, average ages and (d) cathodoluminescence images of representative zircon grains for the Guyong monzogranite and Xiaolonghe medium- and fine-grained syenogranite. For (d), the yellow circles represent U–Pb age spots; the dashed red circles represent Lu–Hf isotope spots; and the green circles represent O isotope spots.

286.54–396.82 ppm (average 341.52 ppm) and 243.93–252.78 ppm (average 248.35 ppm), respectively. The light REE/heavy REE (LREE/HREE) ratios for the GPM, XMS and XFS are in the range of 8.74–10.47 (average 9.49), 4.96–6.58 (average 5.65) and 1.50–1.95 (average 1.73), respectively; the $(La/Yb)_N$ ratios are 7.84–10.77 (average 9.45), 4.54–6.32 (average 5.25) and 0.70–0.92 (average 0.81), respectively; and the δEu values are in the range of 0.28–0.37, 0.058–0.079 and 0.008–0.012, respectively. In the chondrite-normalized REE diagram, the GPM shows rightward slope patterns and slight negative Eu anomalies. Compared with the GPM, the XMS shows higher HREE contents and obvious negative Eu anomalies, but the LREE contents do not show much variation (Fig. 7a). The XFS shows the lowest LREE and highest HREE contents, with marked negative Eu anomalies compared with the former two granites, which exhibit a relatively flat 'seagull' pattern. An apparent tetrad effect is clearly observed in the M-shaped REE patterns of the XFS, with four convex curves defined by La–Ce–Pr–Nd, (Pm)–Sm–Eu–Gd, Gd–Tb–Dy–Ho and Er–Tm–Yb–Lu. The most abundant elements for each group of convex curves previously mentioned are Ce, Sm, Dy and Yb, respectively. All samples of the granitoids are depleted in Ba, Sr, P and Ti, and the degree of depletion increases from the GPM to the XMS and XFS, as seen in the primitive mantle-normalized trace-element spider diagram. The LILEs (e.g. Rb and U) and Ta show enrichment, whereas Zr shows a decrease from the GPM to the XMS and XFS (Fig. 7b).

4.d. Sr–Nd isotopes

The whole-rock Sr–Nd isotopic compositions of three samples for the GPM are listed in Table 1. The initial $^{87}Sr/^{86}Sr$ ratios (I_{Sr}) and whole-rock εNd(*t*) isotopic values were calculated based on the emplacement age of 76 Ma. The GPM has relatively higher I_{Sr} ratios (0.7098–0.7099), with whole-rock εNd(*t*) isotopic values in the range of −9.7 to −10.1, and single-stage Nd model ages of 1.56–1.63 Ga.

5. Discussion

5.a. Petrogenesis of monzogranite

The compositional variations in granitoids are mainly controlled by partial melting and fractional crystallization (Gao *et al.* 2016;

https://doi.org/10.1017/S0016756819001493 Published online by Cambridge University Press

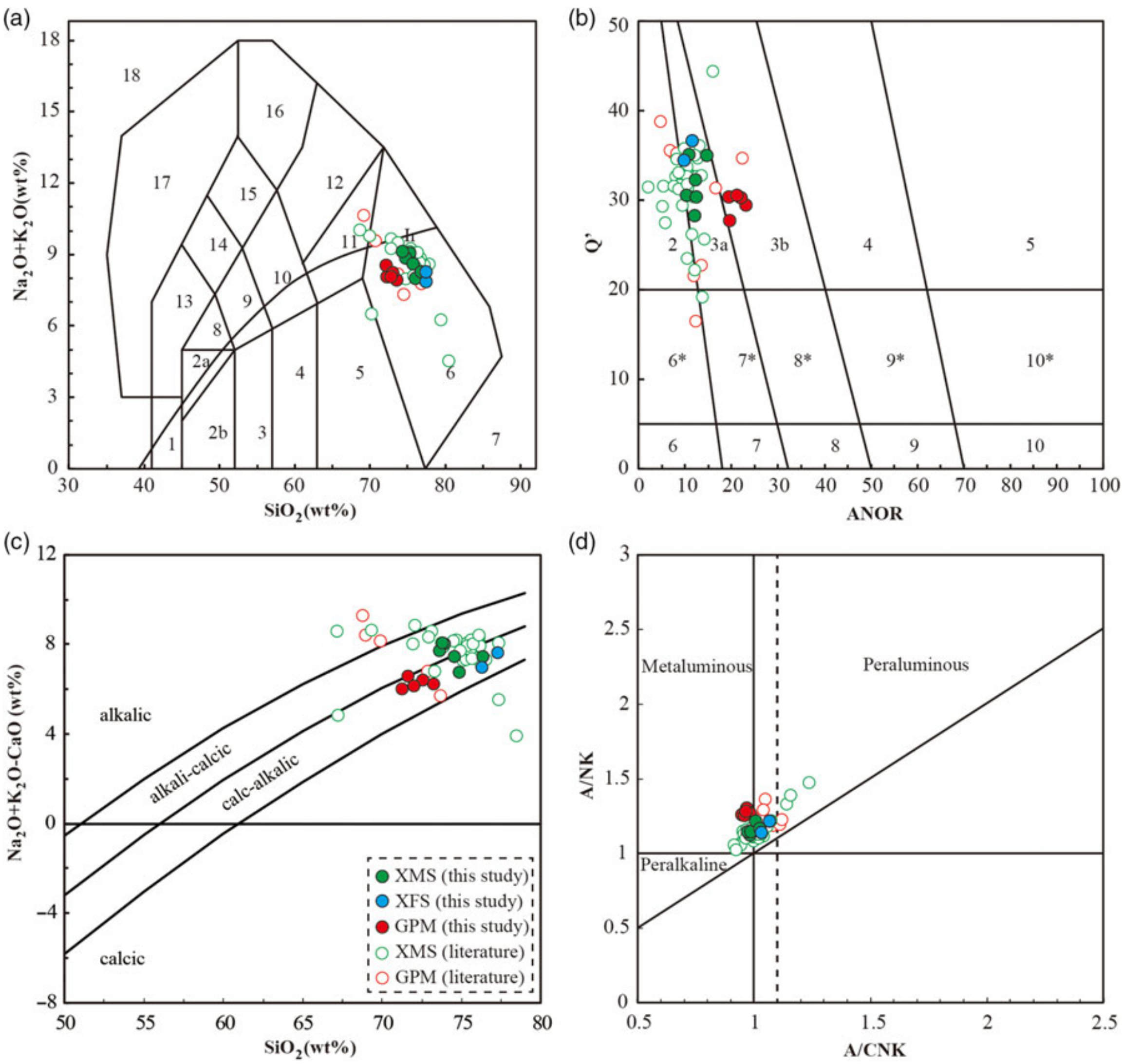

Fig. 5. (Colour online) (a) Total alkalis ($K_2O + Na_2O$) versus SiO_2 (TAS) diagram (Middlemost, 1994). (b) Q′–ANOR classification diagram (Streckeisen & Le Maitre, 1979); ANOR = An/(Or + An) × 100; Q′ = Q/(Q + Or + Ab + An) × 100. (c) ($Na_2O + K_2O$ − CaO) versus SiO_2 diagram (Frost *et al.* 2001). (d) A/NK versus A/CNK diagram (Maniar & Piccoli, 1989). For (a): 1 – peridotgabbro; 2 – gabbro; 3 – gabbroic diorite; 4 – diorite; 5 – granodiorite; 6 – granite; 7 – quartzolite; 8 – monzogabbro; 9 – monzodiorite; 10 – monzonite; 11 – quartz monzonite; 12 – syenite; 13 – foid gabbro; 14 – foid monzodiorite; 15 – foid monzosyenite; 16 – foid syenite; 17 – foidolite; 18 – tawite/urtite/italite. For (b): 2 – alkalic feldspar granite; 3a – syenogranite/granite; 3b – monzogranite; 4 – granodiorite; 5 – tonalite; 6* – quartz alkali feldspar syenite; 7* – quartz monzonite; 8* – quartz monzodiorite; 9* – quartz monzodiorite/quartz monzogabbro; 10* – quartz diorite/quartz gabbro/quartz anorthosite; 6 – alkali feldspar syenite; 7 – syenite; 8 – monzonite; 9 – monzodiorite/monzogabbro; 10 – diorite/gabbro/anorthosite. Data sources: Jiang *et al.* (2012); Zhang *et al.* (2013); Cao (2015); Chen, X. C. *et al.* (2015); Qi *et al.* (2015); Cao *et al.* (2016); Dong (2016); Yu (2016); Zhao *et al.* (2017*b*).

Zhang *et al.* 2019). All samples from the GPM, XMS and XFS have high Rb/Sr ratios and low Sr contents, which cannot be generated by equilibrium partial melting, and they require fractional crystallization (Halliday *et al.* 1991). Moreover, the high differentiation index values of the XMS (91.06–94.35) and XFS (93.58–95.04) also indicate that they have experienced fractional crystallization. The U–Pb ages of the GPM, XMS and XFS are consistent (75.9 Ma, 75.6 Ma and 75.7 Ma, respectively), which suggests that they were derived from the same batch of magma (Zhang, Q. W. *et al.* 2018). Therefore, we consider these intrusions to be cogenetic, and the XMS and XFS represent the fractionated products of the GPM.

Granites cannot be generated by direct melting of the mantle, and the major mechanism that produces granitic magmas is partial melting of crustal rocks (Brown, 2013; Gao *et al.* 2016; Scaillet *et al.* 2016). The GPM is most close to the initial melt composition compared to the XMS and XFS because of crystal fractionation (Sawyer *et al.* 2011). From Figure 7a, it is seen that the GPM is more enriched than the upper crust, and its enrichment in LREEs and depletion in Eu possibly results from anatexis of the lower crust (Sawyer *et al.* 2011; Brown, 2013; Wu *et al.* 2017). To further constrain the source region of the GPM, we evaluated the zircon Hf–O for all of the samples and the whole-rock Sr–Nd isotopes for the GPM due to the XMS. It was found that the XFS has high Rb/Sr ratios and shows unreasonably high initial $^{87}Sr/^{86}Sr$ ratios with a wide range (Chen, X. C. *et al.* 2015). The GPM has similar Sr–Nd isotope characteristics as the Early Cretaceous granites (Fig. 8) derived from ancient lower crust in the east Tengchong Block and Gaoligong belt (Yang *et al.* 2006; Zhu *et al.* 2015, 2017*a*, 2018*a*,*b*; Zhao *et al.* 2016*b*, 2017*a*; Zhu, 2017; Wan, 2018; Wan *et al.* 2018; Zhang, J. Y. *et al.* 2018). The GPM is different from the Eocene granitic rocks in the west Tengchong Block with diverse Sr–Nd isotope values (Fig. 8), which were derived from ancient crust (Wu, 2014;

https://doi.org/10.1017/S0016756819001493 Published online by Cambridge University Press

Table 1. Whole-rock Sr–Nd isotopic data for the Guyong monzogranite.

Samples	Rb (ppm)	Sr (ppm)	$^{87}Rb/^{86}Sr$	$^{87}Sr/^{86}Sr$	2σ	$^{87}Sr/^{86}Sr(t)$	Sm (ppm)	Nd (ppm)	$^{147}Sm/^{144}Nd$	$^{143}Nd/^{144}Nd$	2σ	T_{DM} (Ma)	εNd(t)
16GY28	406	178	6.5	0.716789	10	0.7098	9.14	48.6	0.113640	0.512081	9	1627	−10.1
16GY42	405	193	5.9	0.716324	9	0.7099	8.57	46.7	0.110985	0.512097	9	1561	−9.7
16GY44	406	177	6.5	0.716955	9	0.7099	8.08	43.1	0.113455	0.512099	8	1596	−9.7

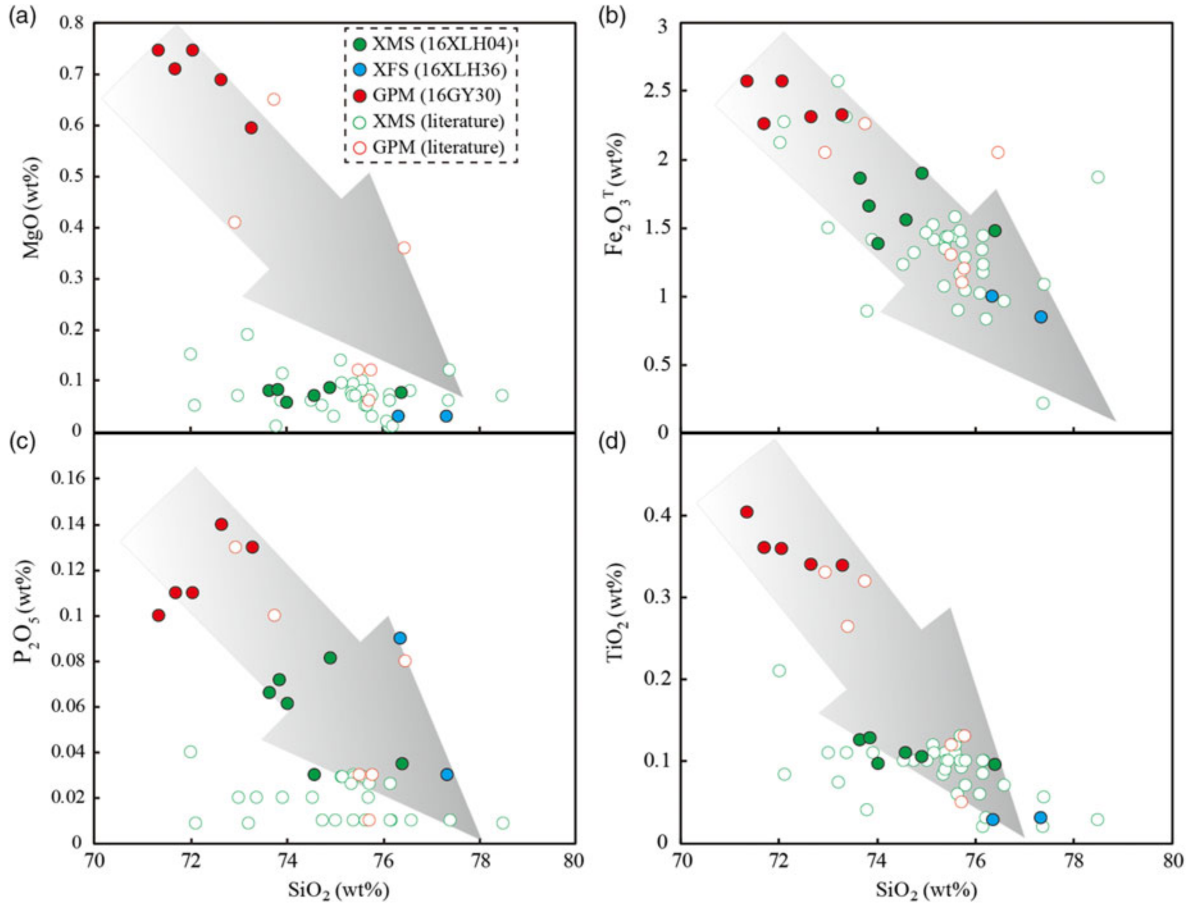

Fig. 6. (Colour online) Variation diagrams of major elements versus SiO_2. (a) MgO; (b) $Fe_2O_3^T$; (c) P_2O_5; (d) TiO_2.

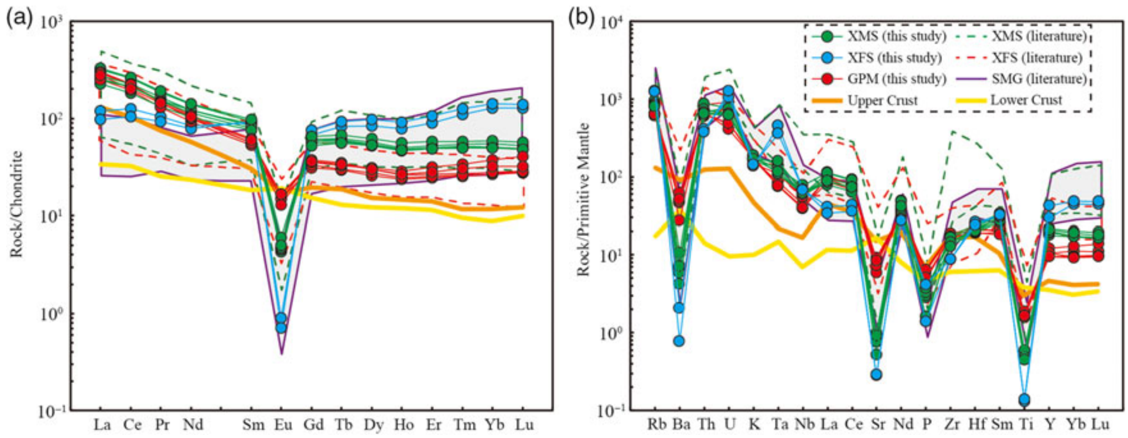

Fig. 7. (Colour online) (a) Chondrite-normalized rare earth element (REE) patterns and (b) primitive mantle-normalized multi-element patterns for the Guyong monzogranite and Xiaolonghe medium- and fine-grained syenogranite. Symbols are the same as Figure 5. Chondrite-normalized and primitive mantle-normalized data are from Sun & McDonough (1989). The data for the crust are from Rudnick & Gao (2003); the data for the SMG are from Jiang *et al.* (2017) and Li *et al.* (2018); the other data sources are the same as those in Figure 5.

https://doi.org/10.1017/S0016756819001493 Published online by Cambridge University Press

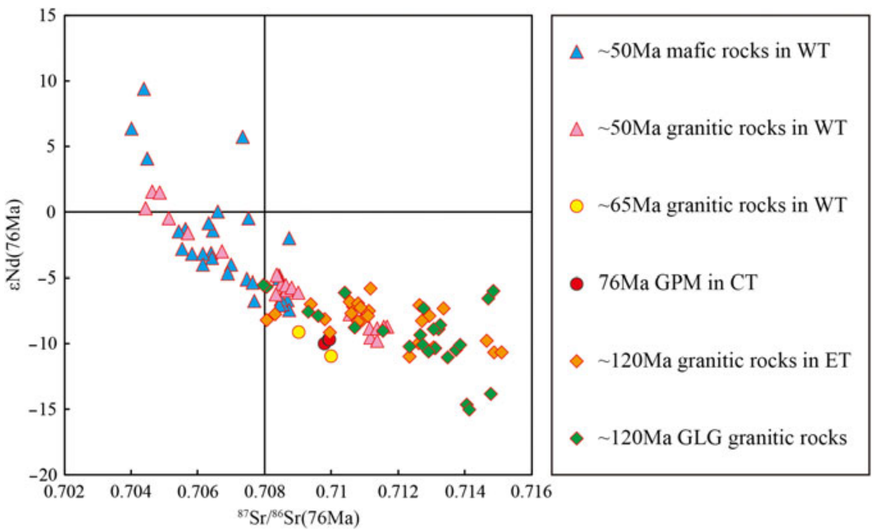

Fig. 8. (Colour online) Whole-rock εNd(t) values versus initial $^{87}Sr/^{86}Sr$ values for the Guyong monzogranite from this study (GPM; circles with black border) and intrusive rocks varying from mafic to felsic in the Tengchong Block from the literature (Ji *et al.* 2000; Yang *et al.* 2006, 2009; Xu *et al.* 2008; Ma *et al.* 2013, 2014; Wang *et al.* 2014, 2015; Wu, 2014; Zhu *et al.* 2015, 2017*a*; 2018*a*,*b*; Zhao *et al.* 2016*a*,*b*, 2017*a*,*b*, 2019; Zhu, 2017; Wan, 2018; Wan *et al.* 2018; Zhang, J. Y. *et al.* 2018) (shapes with red border, all the data are recalculated for the age of 76 Ma). Abbreviations: WT – West Tengchong; CT – Central Tengchong; ET – East Tengchong; GLG – Gaoligong.

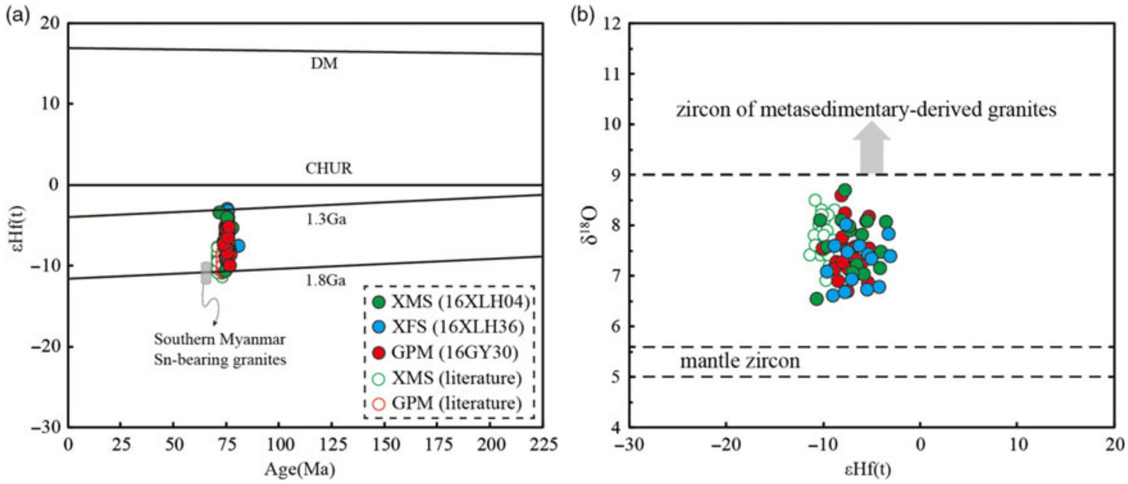

Fig. 9. (Colour online) (a) Zircon εHf(t) values versus U–Pb ages (Ma); (b) zircon $\delta^{18}O$ values versus εHf(t) values for the Guyong monzogranite and Xiaolonghe medium- and fine-grained syenogranite. Fields in (b) are from Kemp *et al.* (2006) and Kemp *et al.* (2007). The data for the SMG are from Jiang *et al.* (2017).

Zhao *et al.* 2016*a*, 2019) or mixed source regions composed of both ancient and juvenile crustal rocks (Ma *et al.* 2014). Thus, the high initial $^{87}Sr/^{86}Sr$ ratios (from 0.7098 to 0.7099) of the GPM (Fig. 8) together with the negative whole-rock εNd(t) isotopic values (from −9.7 to −10.1) indicate that they were generated by partial melting of ancient lower crust.

All zircon εHf(t) isotopic values of the GPM, XMS and XFS are negative and below the value of CHUR (chondritic uniform reservoir) (Fig. 9a), and they show similarity with the Southern Myanmar Sn-bearing granites (SMG) that were derived from partial melting of the Palaeoproterozoic continental crust (Jiang *et al.* 2017). This similarity suggests that the magma was derived from an ancient crustal source. As all the $^{147}Sm/^{144}Nd$ ratios are between 0.13 and 0.10, the single-stage Nd model ages (~1.6 Ga) that are consistent with the two-stage Hf model ages (from 1.5 to 1.8 Ga for GPM, 1.4 to 1.8 Ga for XMS, and 1.3 to 1.8 Ga for XFS) can represent the age of the source region (Li, 1996). Therefore, the parental magma of the GPM was generated by partial melting of ancient crust separated from depleted mantle during Mesoproterozoic times (Yang *et al.* 2007; Qi *et al.* 2015). According to Li *et al.* (2016), the Gaoligong metamorphic complex shows four age peaks in the Neoarchaean (~2.5 Ga), Mesoproterozoic (~1.6 Ga), Grenvillian (~1.17 Ga and 0.95 Ga) and Late Neoproterozoic – Cambrian (0.65–0.5 Ga). In summary, together with the presence of an inherited zircon of 929 Ma from the GPM, we consider that the magma that formed the GPM was generated by partial melting of the Proterozoic Gaoligong metamorphic complex.

The GPM has brown biotite, rare amphibole and inherited zircon with accessory minerals of titanite, which show the characteristics of I-type granites (Brown, 2013; Gao *et al.* 2016; Jagoutz & Klein, 2018; Jeon & Williams, 2018). The similar $\delta^{18}O$ values of the GPM, XMS and XFS (between 6.5 ‰ and 9 ‰; Fig. 9b) and the wide range in zircon εHf(t) isotopic values (between −10.04 and −3.04) suggest that they are connected and their source region incorporates metasedimentary and meta-igneous rocks (Kemp *et al.* 2006; Gardiner *et al.* 2017; Yang *et al.* 2017). Therefore, the GPM was generated by the partial melting of the metasedimentary and meta-igneous rocks from the Gaoligong crystalline basement.

5.b. Fractional crystallization

From analysis of the change in the geochemical compositions, we can infer the detailed processes of fractional crystallization.

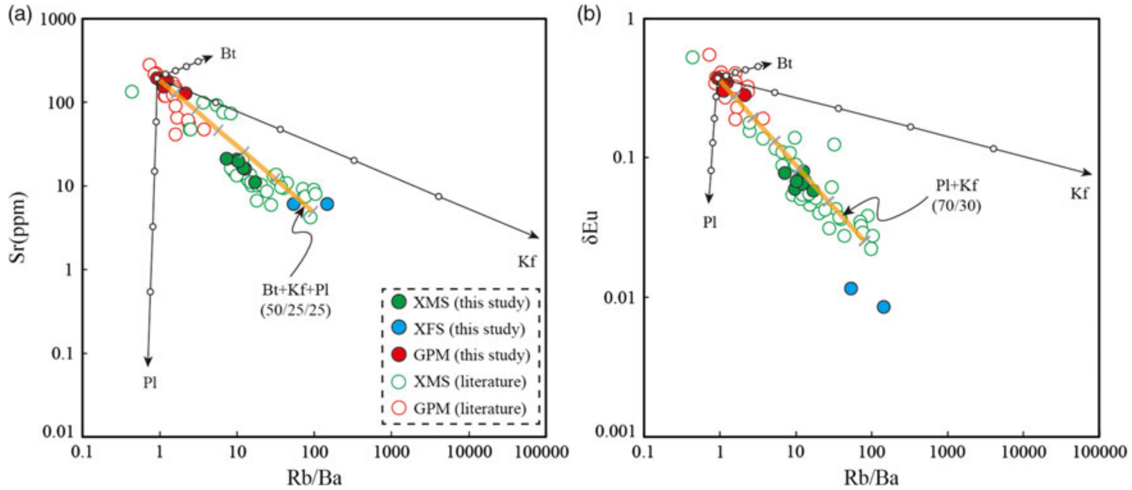

Fig. 10. (Colour online) (a) Sr contents (ppm) versus Rb/Ba ratios; (b) Eu anomalies (δEu) versus Rb/Ba ratios for the Guyong monzogranite and Xiaolonghe medium- and fine-grained syenogranite. The partition coefficients for biotite, K-feldspar and plagioclase are based on Bachmann *et al.* (2005). White circles and blue lines on vectors show 10 % fractionation increments. Abbreviations: Bt – biotite; Kf – K-feldspar; Pl – plagioclase. The data sources are the same as those in Figure 5.

Although the contents of Rb, U and Ta increase and those of Ba, Sr, P, Zr, Ti and Eu decrease from the GPM to the XMS and XFS (Fig. 7b), the trace-element ratios of Rb/Sr, Rb/Ba, Zr/Hf and Nb/Ta are more appropriate to evaluate the degree of fractional crystallization (Halliday *et al.* 1991; Deering & Bachmann, 2010; Stepanov *et al.* 2014; Ballouard *et al.* 2016; Wu *et al.* 2017). It is clear from Figure 10 that there is an increase in Rb/Ba ratio from the monzogranite to the syenogranite, indicating fractionation of biotite and K-feldspar. The marked negative Eu anomalies and the decrease in Sr content suggest the control of plagioclase and K-feldspar. The increase in Rb/Ba ratio can result from the fractionation of either biotite and K-feldspar with a 2:1 ratio (Fig. 10a) or by K-feldspar alone (Fig. 10b). Based on our petrographic observation, the increase in Rb/Ba ratio is correlated to biotite and K-feldspar rather than to K-feldspar only. Since it is difficult to generate prominent negative Eu anomalies from the fractionation of plagioclase alone (Figs 7a, 10b), we consider that the decrease in Sr content (Fig. 10a) and δEu are induced by the fractionation of both plagioclase and K-feldspar. The decrease in Zr/Hf ratios is correlated with the fractional crystallization of zircon (Deering & Bachmann, 2010; Dostal *et al.* 2015; Zhang *et al.* 2019), which is also consistent with the decrease in zircon content from the GPM to the XMS and XFS. As shown in Figure 7a, the GPM and XMS have similar LREE contents, but the XFS has relatively lower LREE contents, and the HREE contents increase gradually, resulting in the change in slopes of the REE patterns from steeply negative to nearly flat. In most granitoids, the majority of the REEs are carried by accessory minerals, and monazite and allanite are extremely rich in LREEs. The decrease in LREE content in the XFS may be related to the fractional crystallization of these two minerals (Miller & Mittlefehldt, 1982, 1984; Fisher *et al.* 2017; Zhang *et al.* 2019). Because HREEs are not strongly concentrated in these minerals, which cause the depletion of LREEs, they behave as incompatible elements, and their concentrations gradually increase from the GPM to the XMS and XFS (Miller & Mittlefehldt, 1984).

The contents of MgO and $Fe_2O_3^T$ clearly decrease with the increase in SiO_2 (Fig. 6a, b) from the GPM to the XMS and XFS, which indicates the fractional crystallization of ferromagnesian minerals (mostly biotites) (Miller & Mittlefehldt, 1984). The saturation of apatite in the GPM caused a rapid decrease in P content from the GPM to the XMS and XFS with further fractional crystallization (Fig. 6c; Lee & Bachmann, 2014). The TiO_2 clearly decreases with the increase in SiO_2 (Fig. 6d) and with the depletion of Ti (Fig. 7b) from the GPM to the XMS and XFS, and this outcome indicates the fractional crystallization of Ti-bearing oxides, such as ilmenite and titanite (Liu *et al.* 2009; Stepanov *et al.* 2014). Ti-bearing oxides or silicates (micas and amphiboles) are the major hosts for Ta and Nb in granites (Stepanov *et al.* 2014; Tang *et al.* 2019). According to Stepanov *et al.* (2014), fractionation of Ti-bearing oxides decreases the Ta/Nb ratios and Ta content (ilmenite and titanite), whereas biotite increases the Ta/Nb ratios and Ta content. The slight increase in Ta content and Ta/Nb ratios with decreasing Ti from the GPM to the XMS is significantly different from the trends displayed by fractionation of ilmenite and titanite (Fig. 11). Thus, the Ta–Nb distinction between the GPM and XMS is accounted for by the fractionation of biotite (Stepanov *et al.* 2014).

In summary, the GPM, XMS and XFS were probably derived from the same batch of magma, and the difference in composition is attributed to the fractional crystallization of biotite, plagioclase, K-feldspar, apatite, ilmenite and titanite. The MUSH model can be invoked in this case, where crystal mush (crystals + melt) crystallized to form a granite rich in K-feldspar phenocrysts (GPM), whereas the residual melt extracted from the mush zone generated the XMS and XFS (Lee & Bachmann, 2014; Lee & Morton, 2015; Wu *et al.* 2017).

5.c. Metallogenic implications

The U–Pb ages of cassiterite (72–74 Ma) and $^{40}Ar–^{39}Ar$ ages of muscovite (72–73 Ma) from the Xiaolonghe tin deposit (Chen *et al.* 2014; Cao *et al.* 2016) indicate that the deposit formed simultaneously with the Guyong and Xiaolonghe plutons (Xu *et al.* 2012; Chen, X. C. *et al.* 2015; Qi *et al.* 2015; Xie *et al.* 2016), and this outcome implies a genetic relationship between the tin deposit and magmatism (Cao *et al.* 2018). Previous studies regarded the XMS to be genetically related to the tin deposit from the perspective of formation age and stable isotopic (C–H–O–S–Pb–He–Ar) compositions (Cao *et al.* 2016; Chen *et al.* 2018); little attention was

https://doi.org/10.1017/S0016756819001493 Published online by Cambridge University Press

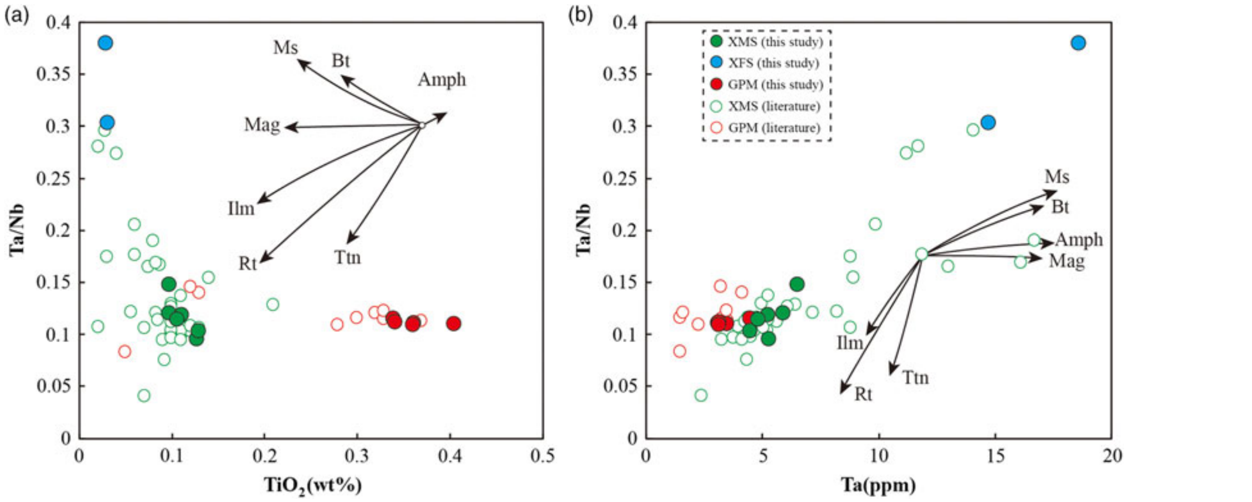

Fig. 11. (Colour online) (a) Ta/Nb ratios versus TiO_2 contents (wt %); (b) Ta/Nb ratios versus Ta contents (ppm) for the Guyong monzogranite and Xiaolonghe medium- and fine-grained syenogranite (Stepanov *et al.* 2014). Abbreviations: Bt – biotite; Ms – muscovite; Mag – magnetite; Ilm – ilmenite; Rt – rutile; Ttn – titanite; Amph – amphibole. The data sources are the same as those in Figure 5.

paid to the relationship between the XFS and tin mineralization. The granites from the Guyong and Xiaolonghe plutons have relatively high Sn contents (8.14–12.3 ppm for GPM, 8.72–21.1 ppm for XMS, and 11.0–20.2 ppm for XFS), which are higher than normal granites without tin mineralization (4.3 ppm; Tischendorf, 1977), and the Sn contents of the Xiaolonghe granites (XMS and XFS) are closer to those of Sn specialized granites (Sn ≥15; Neiva, 1984; Fig. 12); this outcome suggests that the Xiaolonghe granites have more Sn metallogenic potential. Ore-forming granites crystallize from silicate melt in the latest stage of crystallization differentiation, which generates volatiles through exsolution and changes the magma system from crystal–melt interaction to crystal–melt–magmatic volatile interaction (Lehmann, 1990; Halter & Webster, 2004). The Sn contents increase with the increase in SiO_2 from the GPM to the XMS and XFS (Fig. 12), indicating that the fractionation of magma can enhance the concentrations of Sn in the residual melt, which is a necessary precursor for the mineralization and formation of tin deposits (Mustard *et al.* 2006; Gardiner *et al.* 2017). The XFS has a similar Sn content as the XMS, indicating that the Sn concentration might reach a critical threshold for exsolution from melt to fluid (Gardiner *et al.* 2017).

The tetrad effect of granites is an efficacious indicator of the metallogenic potential of rare metals (Irber, 1999; Monecke *et al.* 2007; Yang *et al.* 2018). Figure 13a shows that as the Nb/Ta ratios decrease, the degree of the tetrad effect (TE_{1-3}) quantified by Irber (1999) increases significantly from the GPM to the XMS and XFS. The XFS displays a high tetrad effect ($TE_{1-3} > 1.1$) with low Nb/Ta ratios (<~5), which are similar to the SMG (Jiang *et al.* 2017; Li *et al.* 2018), and this outcome suggests an interaction between magma and fluids (Ballouard *et al.* 2016). The Zr/Hf ratio is also a marker of either fractional crystallization or magmatic–hydrothermal interactions (Ballouard *et al.* 2016). In Figure 13b, the XFS shows similar characteristics to the SMG and belongs to the field of rare metal-related granites (Ta–Cs–Li–Nb–Be–Sn–W); both the GPM and XMS belong to the field of barren granites. In addition, the average zircon δEu values of the GPM and XMS are greater than 0.08 (online Supplementary Material Table S4), which are similar to barren granites (Gardiner *et al.* 2017); meanwhile, those of the XFS are equal to or less than 0.08, which indicates tin-producing granites. Therefore, we

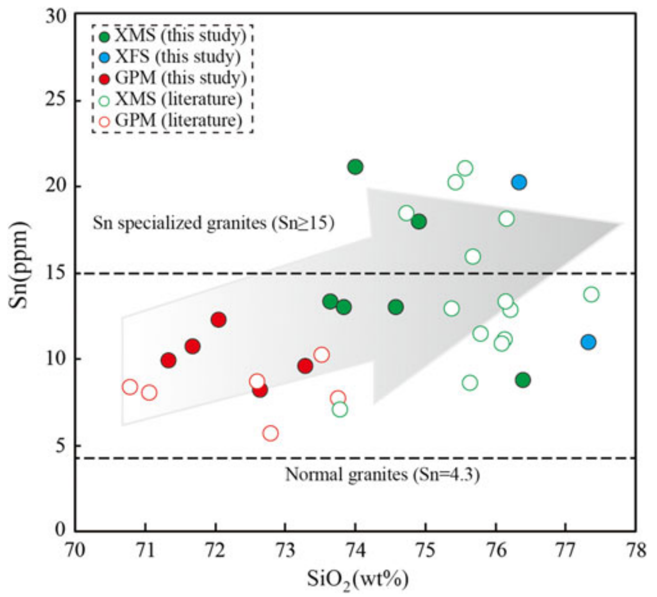

Fig. 12. (Colour online) Evolution of Sn contents (ppm) versus SiO_2 contents (wt %) for the Guyong monzogranite and Xiaolonghe medium- and fine-grained syenogranite. The green hollow circles represent the data from Chen, X. C. *et al.* (2015) and the red hollow circles represent our unpublished data. The Sn content of normal granites is from Tischendorf (1977) and the specialized granites is from Neiva (1984); the other data sources are the same as those in Figure 5.

conclude that the latest XFS is an ore-forming intrusion and that Sn is scavenged by the exsolved hydrothermal fluids.

5.d. Tectonic implications

Granites can be produced in diverse tectonic settings, such as continental collisions, continental rifts, post-continental settings and subduction zones (Jagoutz & Klein, 2018). The main arguments about the tectonic setting of the Tengchong Late Cretaceous granites in previous studies are as follows: (1) The culmination of crustal thickening, induced by the eastward subduction of the Neo-Tethys and plate convergence, and subsequent extensional collapse led to the generation of the Late Cretaceous

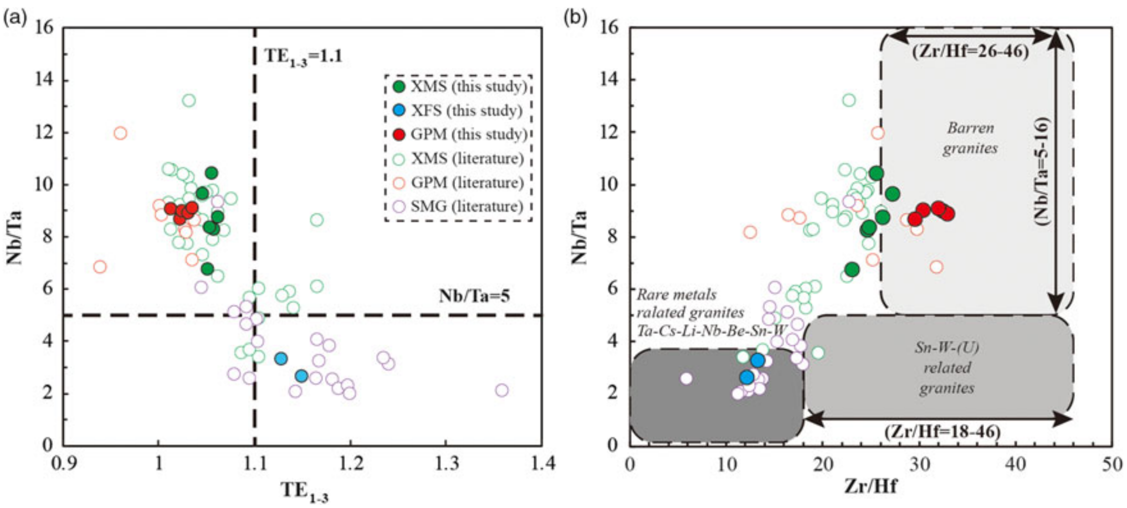

Fig. 13. (Colour online) (a) Evolution of Nb/Ta ratios versus degree of tetrad effect (TE_{1-3}); (b) Nb/Ta ratios versus Zr/Hf ratios diagram to differentiate barren and ore-forming granites for the Guyong monzogranite and Xiaolonghe medium- and fine-grained syenogranite (Ballouard *et al.* 2016). The data for the SMG are from Jiang *et al.* (2017) and Li *et al.* (2018); the other data sources are the same as those in Figure 5.

granites in the Tengchong Block (Xu *et al.* 2012; Ma *et al.* 2013; Cao *et al.* 2019); (2) underplating of basaltic magma generated by partial melting of the mantle during the eastward subduction of the Neo-Tethys resulted in the melting of the thickened lower crust which formed the Late Cretaceous granites in the Tengchong Block (Yang *et al.* 2009); (3) the Tengchong Late Cretaceous granites are A-type granites generated during the post-orogenic extension stage after collision of the Tengchong and Baoshan blocks (Jiang *et al.* 2012; Zhang *et al.* 2013); (4) the collision between the Tengchong and Burma blocks along with subduction of the Neo-Tethys caused the thickening of crust, and subsequent extensional collapse during Late Cretaceous times produced the Xiaolonghe granites (Chen, X. C. *et al.* 2015).

The Tengchong Block and Mogok–Mandalay–Mergui belt in the SE Asian tin belt have been structurally linked since Early Cretaceous times (Xu *et al.* 2015). The Late Cretaceous SMG are typical Sn-bearing granites from the SE Asian tin belt and are mostly derived from the partial melting of ancient crust during the subduction of the Neo-Tethys Ocean (Jiang *et al.* 2017; Myint *et al.* 2017; Li *et al.* 2018). The certain geochemical similarities of the Late Cretaceous granites suggest a genetic link between them (Figs 7, 9, 13). Furthermore, some of the Late Cretaceous deposits from the SE Asian tin belt and the Xiaolonghe deposit have almost the same metallogenic ages (Cao *et al.* 2016; Gardiner *et al.* 2016). Therefore, the geochronological and geochemical evidence indicates that they experienced consistent tectono-magmatic histories during Late Cretaceous times (Cao *et al.* 2016; Xie *et al.* 2016).

The geothermal gradients of 20 °C km^{-1} cannot generate enough heat for the melting of crustal rocks (Petford *et al.* 2000). Therefore, an external heat source for the melting of crustal rocks is required. Although granitic rocks cannot be generated by the partial melting of mantle peridotite, asthenosphere upwelling in the orogenic belt can provide thermal input for the melting of crustal rocks. The mafic dykes in the Lianghe area generated by the partial melting of upwelling asthenosphere indicate the break-off of the Neo-Tethys slab at ~40 Ma beneath the Tengchong Block (Xu *et al.* 2008). Wang *et al.* (2014) considered that the rollback of the Neo-Tethys slab beneath the west Tengchong Block during ~55–50 Ma marks the transition from subduction to initial collision of India–Asia. Ma *et al.* (2014) considered that the juvenile mantle-derived basaltic magma underplating the ancient crust beneath the west Tengchong Block during ~60–70 Ma resulted from the subduction of the Neo-Tethys, and the initiation of the collision of India–Asia was not earlier than ~55 Ma. The upwelling and underplating of mantle-derived magma induced by subduction of the Neo-Tethys provided the heat source for the partial melting of crustal rocks (Chen, X. C. *et al.* 2015; Jiang *et al.* 2017). The subduction of the Neo-Tethys beneath the Tengchong Block changed from flat to steep, and the convergence rate increased rapidly from *c.* 70 Ma (Cao *et al.* 2018). Thus, we consider that the Late Cretaceous (~75 Ma) magma in the central Tengchong Block was produced by the change in subduction angle, which resulted in the upwelling of the asthenosphere that provided heat for the melting of crustal rocks. For the SMG, the heat is also provided by the upwelling of the asthenosphere that is induced by the rollback of the Neo-Tethyan subducting slab (Jiang *et al.* 2017; Myint *et al.* 2017). Correlating the ages of the Tengchong Late Cretaceous granites and the SMG (Cao *et al.* 2016; Jiang *et al.* 2017), we propose that the subduction of the Neo-Tethys resulted in the upwelling of the asthenosphere and subsequent partial melting of the lower crust, resulting in the formation of the parental magma of the Tengchong Late Cretaceous granites and the SMG. Then, the process of fractional crystallization led to the enrichment of Sn and the generation of Sn-bearing granites.

6. Conclusions

The key results from this study are as follows.

(1) Compared with the GPM, the XMS and XFS have more quartz, less feldspar and biotite, and show strong depletion in Eu, Ba, Sr, P and Ti and relative enrichment of HREEs, Rb and Ta.
(2) The parental magma of the GPM was derived from the partial melting of ancient crust in the Tengchong Block. The XMS and XFS are considered products of differentiation of the GPM through the fractionation of feldspars, apatite, biotite, apatite, ilmenite and titanite.

https://doi.org/10.1017/S0016756819001493 Published online by Cambridge University Press

(3) The XFS is regarded as the ore-forming granite, and Sn was scavenged by exsolved hydrothermal fluids.
(4) The Late Cretaceous magmatic activities in the Tengchong Block were related to the subduction of the Neo-Tethys, which resulted in the upwelling of the asthenosphere and subsequent partial melting of the lower crust.

Supplementary Material. To view supplementary material for this article, please visit https://doi.org/10.1017/S0016756819001493

Acknowledgements. This work was supported by The National Key Research and Development Program (Grant No. 2016YFC0600502) and National Science Foundation (9175520034) of China. The two anonymous referees and editor Kathryn Goodenough are also thanked for offering constructive comments and suggestions for improving this manuscript.

References

Andersen T (2002) Correction of common lead in U–Pb analyses that do not report ^{204}Pb. *Chemical Geology* **192**, 59–79.

Bachmann O, Dungan MA and Bussy F (2005) Insights into shallow magmatic processes in large silicic magma bodies: the trace element record in the Fish Canyon magma body, Colorado. *Contributions to Mineralogy and Petrology* **149**, 338–49.

Ballouard C, Poujol M, Boulvais P, Branquet Y, Tartese R and Vigneresse JL (2016) Nb–Ta fractionation in peraluminous granites: a marker of the magmatic-hydrothermal transition. *Geology* **44**, 231–4.

Brown M (2013) Granite: from genesis to emplacement. *Geological Society of America Bulletin* **125**, 1079–113.

Cao HW (2015) Research on Mesozoic–Cenozoic magmatic evolution and its relation with metallogeny in Tengchong-Lianghe tin ore belt, western Yunnan. Ph.D. thesis, China University of Geosciences (Beijing), Beijing, China, 349 pp. Published thesis.

Cao HW, Pei QM, Zhang ST, Zhang LK, Tang L, Lin JZ and Zheng L (2017a) Geology, geochemistry and genesis of the Eocene Lailishan Sn deposit in the Sanjiang region, SW China. *Journal of Asian Earth Sciences* **137**, 220–40.

Cao HW, Zhang ST, Lin JZ, Zheng L, Wu JD and Li D (2014) Geology, geochemistry and geochronology of the Jiaojiguanliangzi Fe-polymetallic deposit, Tengchong County, Western Yunnan (China): regional tectonic implications. *Journal of Asian Earth Sciences* **81**, 142–52.

Cao HW, Zhang YH, Pei QM, Zhang RQ, Tang L, Lin B and Cai GJ (2017b) U–Pb dating of zircon and cassiterite from the Early Cretaceous Jiaojiguan iron-tin polymetallic deposit, implications for magmatism and metallogeny of the Tengchong area, western Yunnan, China. *International Geology Review* **59**, 234–58.

Cao HW, Zhang YH, Santosh M, Zhang ST, Tang L, Pei QM and Yang QY (2018) Mineralogy, zircon U–Pb–Hf isotopes, and whole-rock geochemistry of Late Cretaceous–Eocene granites from the Tengchong terrane, western Yunnan, China: Record of the closure of the Neo-Tethyan Ocean. *Geological Journal* **53**, 1423–41.

Cao HW, Zhang YH, Tang L, Hollis SP, Zhang ST, Pei QM, Yang C and Zhu XS (2019) Geochemistry, zircon U–Pb geochronology and Hf isotopes of Jurassic–Cretaceous granites in the Tengchong terrane, SW China: implications for the Mesozoic tectono-magmatic evolution of the Eastern Tethyan tectonic domain. *International Geology Review* **61**, 257–79.

Cao HW, Zou H, Zhang YH, Zhang ST, Zheng L, Zhang LK, Tang L and Pei QM (2016) Late Cretaceous magmatism and related metallogeny in the Tengchong area: evidence from geochronological, isotopic and geochemical data from the Xiaolonghe Sn deposit, western Yunnan, China. *Ore Geology Reviews* **78**, 196–212.

Cawood PA and Hawkesworth CJ (2019) Continental crustal volume, thickness and area, and their geodynamic implications. *Gondwana Research* **66**, 116–25.

Chen XC, Hu RZ, Bi XW, Li HM, Lan JB, Zhao CH and Zhu JJ (2014) Cassiterite LA-MC-ICP-MS U/Pb and muscovite ^{40}Ar/^{39}Ar dating of tin deposits in the Tengchong-Lianghe tin district, NW Yunnan, China. *Mineralium Deposita* **49**, 843–60.

Chen XC, Hu RZ, Bi XW, Zhong H, Lan JB, Zhao CH and Zhu JJ (2015) Petrogenesis of metaluminous A-type granitoids in the Tengchong–Lianghe tin belt of southwestern China: evidences from zircon U–Pb ages and Hf–O isotopes, and whole-rock Sr-Nd isotopes. *Lithos* **212–215**, 93–110.

Chen HJ, Zhang ST, Cao HW, Wang XF, Nie XL, Zhang W and Tang L (2015) Compositional characteristics, petrogenesis and metallogenic significance of biotite from granite in the Guyong region of Western Yunnan Province, China. *Acta Mineralogica Sinica* **35**, 267–75 (in Chinese with English abstract).

Chen XC, Zhao CH, Zhang M and Yang W (2017) Sulfur isotope geochemical characteristics of a typical tin deposits in Tengchong-Lianghe tin belt, West Yunnan Province, China. *Acta Mineralogica Sinica* **37**, 705–11 (in Chinese with English abstract).

Chen XC, Zhao CH, Zhu JJ, Wang XS and Cui T (2018) He, Ar, and S isotopic constraints on the relationship between A-type granites and tin mineralization: a case study of tin deposits in the Tengchong–Lianghe tin belt, southwest China. *Ore Geology Reviews* **92**, 416–29.

Cui XL, Wang QF, Deng J, Wu HY and Shu QH (2019) Genesis of the Xiaolonghe quartz vein type Sn deposit, SW China: insights from cathodoluminescence textures and trace elements of quartz, fluid inclusions, and oxygen isotopes. *Ore Geology Reviews* **111**, 102929. doi: 10.1016/j.oregeorev.2019.05.015.

Deering CD and Bachmann O (2010) Trace element indicators of crystal accumulation in silicic igneous rocks. *Earth and Planetary Science Letters* **297**, 324–31.

Deng J, Wang QF, Li GJ, Li CS and Wang CM (2014) Tethys tectonic evolution and its bearing on the distribution of important mineral deposits in the Sanjiang region, SW China. *Gondwana Research* **26**, 419–37.

Dong ML (2016) *Study of magmatism in Tengchong-Baoshan Block, western Yunnan and its tectonic implications.* Ph.D. thesis, China University of Geosciences (Beijing), Beijing, China, 186 pp. Published thesis.

Dostal J, Kontak DJ, Gerel O, Shellnutt GJ and Fayek M (2015) Cretaceous ongonites (topaz-bearing albite-rich microleucogranites) from Ongon Khairkhan, Central Mongolia: products of extreme magmatic fractionation and pervasive metasomatic fluid: rock interaction. *Lithos* **236–237**, 173–89.

Elhlou S, Belousova E, Griffin WL, Pearson NJ and O'Reilly SY (2006) Trace element and isotopic composition of GJ-red zircon standard by laser ablation. *Geochimica et Cosmochimica Acta* **70**, A158.

Fang Y, Zhang YH, Zhang ST, Cao HW, Zou H and Dong JH (2018) Early Cretaceous I-type granites in the Tengchong terrane: new constraints on the late Mesozoic tectonic evolution of southwestern China. *Geoscience Frontiers* **9**, 459–70.

Fisher CM, Hanchar JM, Miller CF, Phillips S, Vervoort JD and Whitehouse MJ (2017) Combining Nd isotopes in monazite and Hf isotopes in zircon to understand complex open-system processes in granitic magmas. *Geology* **45**, 267–70.

Frost BR, Barnes CG, Collins WJ, Arculus RJ, Ellis D J and Frost CD (2001) A geochemical classification for granitic rocks. *Journal of Petrology* **42**, 2033–48.

Fu B, Broecker M, Ireland T, Holden P and Kinsley LPJ (2015) Zircon U–Pb, O, and Hf isotopic constraints on Mesozoic magmatism in the Cyclades, Aegean Sea, Greece. *International Journal of Earth Sciences* **104**, 75–87.

Gao P, Zheng YF and Zhao ZF (2016) Experimental melts from crustal rocks: a lithochemical constraint on granite petrogenesis. *Lithos* **266–267**, 133–57.

Gardiner NJ, Hawkesworth CJ, Robb LJ, Whitehouse MJ, Roberts NMW, Kirkland CL and Evans NJ (2017) Contrasting granite metallogeny through the zircon record: a case study from Myanmar. *Scientific Reports* **7**, 748. doi: 10.1038/s41598-017-00832-2.

Gardiner NJ, Robb LJ, Morley CK, Searle MP, Cawood PA, Whitehouse MJ, Kirkland CL, Roberts NMW and Myint TA (2016) The tectonic and metallogenic framework of Myanmar: a Tethyan mineral system. *Ore Geology Reviews* **79**, 26–45.

Halliday A, Davidson JP, Hildreth W and Holden P (1991) Modelling the petrogenesis of high Rb/Sr silicic magmas. *Chemical Geology* **92**, 107–14.

Halter WE and Webster JD (2004) The magmatic to hydrothermal transition and its bearing on ore-forming systems. *Chemical Geology* **210**, 1–6.

Hawkesworth C, Cawood PA and Dhuime B (2019) Rates of generation and growth of the continental crust. *Geoscience Frontiers* **10**, 165–73.

Irber W (1999) The lanthanide tetrad effect and its correlation with K/Rb, Eu/Eu*, Sr/Eu, Y/Ho, and Zr/Hf of evolving peraluminous granite suites. *Geochimica et Cosmochimica Acta* **63**, 489–508.

Jagoutz O and Klein B (2018) On the importance of crystallization-differentiation for the generation of SiO_2-rich melts and the compositional build-up of arc (and continental) crust. *American Journal of Science* **318**, 29–63.

Jeon H and Williams IS (2018) Trace inheritance—clarifying the zircon O–Hf isotopic fingerprint of I-type granite sources: implications for the restite model. *Chemical Geology* **476**, 456–68.

Ji JQ, Zhong DL and Chen CY (2000) Geochemistry and genesis of Nabang metamorphic basalt, southwest Yunnan, China: implications for the subducted slab break-off. *Acta Petrologica Sinica* **16**, 433–42 (in Chinese with English abstract).

Jiang B, Gong QJ, Zhang J and Ma N (2012) Late Cretaceous aluminium A-type granites and its geological significance of Dasongpo Sn deposit, Tengchong, West Yunnan. *Acta Petrologica Sinica* **28**, 1477–92 (in Chinese with English abstract).

Jiang H, Li WQ, Jiang SY, Wang H and Wei XP (2017) Geochronological, geochemical and Sr-Nd-Hf isotopic constraints on the petrogenesis of Late Cretaceous A-type granites from the Sibumasu Block, Southern Myanmar, SE Asia. *Lithos* **268–271**, 32–47.

Kemp AI, Hawkesworth CJ, Foster GL, Paterson BA, Woodhead JD, Hergt JM, Gray CM and Whitehouse MJ (2007) Magmatic and crustal differentiation history of granitic rocks from Hf–O isotopes in zircon. *Science* **315**, 980–3.

Kemp AIS, Hawkesworth CJ, Paterson BA and Kinny PD (2006) Episodic growth of the Gondwana supercontinent from hafnium and oxygen isotopes in zircon. *Nature* **439**, 580–3.

Lee C-TA and Bachmann O (2014) How important is the role of crystal fractionation in making intermediate magmas? Insights from Zr and P systematics. *Earth and Planetary Science Letters* **393**, 266–74.

Lee C-TA and Morton DM (2015) High silica granites: terminal porosity and crystal settling in shallow magma chambers. *Earth and Planetary Science Letters* **409**, 23–31.

Lehmann B (1990) *Metallogeny of Tin*. Lecture Notes in Earth Sciences. Berlin: Springer-Verlag.

Li XH (1996) Nd Isotopic evolution of sediments from the southern margin of the Yangtze block and its tectonic significance. *Acta Petrologica Sinica* **12**, 359–69 (in Chinese with English abstract).

Li D, Chen Y, Hou K and Luo Z (2016) Origin and evolution of the Tengchong block, southeastern margin of the Tibetan Plateau: zircon U–Pb and Lu–Hf isotopic evidence from the (meta-) sedimentary rocks and intrusions. *Tectonophysics* **687**, 245–56.

Li H, Myint AZ, Yonezu K, Watanabe K, Algeo TJ and Wu JH (2018) Geochemistry and U–Pb geochronology of the Wagone and Hermyingyi A type granites, southern Myanmar: implications for tectonic setting, magma evolution and Sn–W mineralization. *Ore Geology Reviews* **95**, 575–92.

Liu YS, Gao S, Hu ZC, Gao CG, Zong KQ and Wang DB (2010) Continental and oceanic crust recycling-induced melt-peridotite interactions in the Trans-North China Orogen: U–Pb dating, Hf isotopes and trace elements in zircons from mantle xenoliths. *Journal of Petrology* **51**, 537–71.

Liu S, Hu RZ, Gao S, Feng CX, Huang ZL, Lai SC, Yuan HL, Liu XM, Coulson IM, Feng GY, Wang T and Qi YQ (2009) U–Pb zircon, geochemical and Sr–Nd–Hf isotopic constraints on the age and origin of Early Palaeozoic I-type granite from the Tengchong–Baoshan Block, Western Yunnan Province, SW China. *Journal of Asian Earth Sciences* **36**, 168–82.

Liu WH, Jiang MR, Zhang XJ, Xia Y, Algeo TJ and Li H (2018) An evolving magmatic-hydrothermal system in the formation of the Mesozoic Meishan magnetite-apatite deposit in the Ningwu volcanic basin, eastern China. *Journal of Asian Earth Sciences* **158**, 1–17.

Liu GL, Qin DX and Fan ZG (2005) Tin resource and its sustainable developing in Yunnan Province. *Conservation and Utilization of Mineral Resources* **2**, 9–13 (in Chinese).

Ludwig KR (2003) *User's Manual for Isoplot 3.00: A Geochronological Toolkit for Microsoft Excel*. Berkeley Geochronology Center, Special Publication no. 4.

Ma N, Deng J, Wang QF, Wang CM, Zhang J and Li GJ (2013) Geochronology of the Dasongpo tin deposit, Yunnan Province: evidence from zircon LA-ICP-MS U–Pb ages and cassiterite LA-MC-ICP-MS U–Pb age. *Acta Petrologica Sinica* **29**, 1223–35 (in Chinese with English abstract).

Ma LY, Wang YJ, Fan WM, Geng HY, Cai YF, Zhong H, Liu HC and Xing XW (2014) Petrogenesis of the early Eocene I-type granites in west Yingjiang (SW Yunnan) and its implication for the eastern extension of the Gangdese batholiths. *Gondwana Research* **25**, 401–19.

Maniar PD and Piccoli PM (1989) Tectonic discrimination of granitoids. *Geological Society of America Bulletin* **101**, 635–43.

Middlemost EAK (1994) Naming materials in the magma igneous rock system. *Earth-Science Reviews* **37**, 215–24.

Miller CF and Mittlefehldt DW (1982) Depletion of light rare-earth elements in felsic magmas. *Geology* **10**, 129–33.

Miller CF and Mittlefehldt DW (1984) Extreme fractionation in felsic magma chambers: a product of liquid-state diffusion or fractional crystallization? *Earth and Planetary Science Letters* **68**, 151–8.

Monecke T, Dulski P and Kempe U (2007) Origin of convex tetrads in rare earth element patterns of hydrothermally altered siliceous igneous rocks from the Zinnwald Sn–W deposit, Germany. *Geochimica et Cosmochimica Acta* **71**, 335–53.

Mustard R, Ulrich T, Kamenetsky VS and Mernagh T (2006) Gold and metal enrichment in natural granitic melts during fractional crystallization. *Geology* **34**, 85–8.

Myint AZ, Zaw K, Swe YM, Yonezu K, Cai Y, Manaka T and Watanabe K (2017) Geochemistry and geochronology of granites hosting the Mawchi Sn–W deposit, Myanmar: implications for tectonic setting and granite emplacement. In *Myanmar: Geology, Resources and Tectonics* (eds AJ Barber, K Zaw, MJ Crow), pp. 385–400. Geological Society of London, Memoirs no. 48.

Neiva AMR (1984) Geochemistry of tin-bearing granitic rocks. *Chemical Geology* **43**, 241–56.

Petford N, Cruden AR, McCaffrey KJ and Vigneresse JL (2000) Granite magma formation, transport and emplacement in the Earth's crust. *Nature* **408**, 669–73.

Qi XX, Zhu LH, Grimmer JC and Hu ZC (2015) Tracing the Transhimalayan magmatic belt and the Lhasa block southward using zircon U–Pb, Lu–Hf isotopic and geochemical data: Cretaceous – Cenozoic granitoids in the Tengchong block, Yunnan, China. *Journal of Asian Earth Sciences* **110**, 170–88.

Roberts NMW and Santosh M (2018) Capturing the Mesoarchean emergence of continental crust in the Coorg block, Southern India. *Geophysical Research Letters* **45**, 7444–53.

Rudnick RL and Gao S (2003) Composition of the continental crust. In *The Crust: Treatise on Geochemistry Vol. 3* (eds HD Holland and KK Turekian), pp. 1–64. Oxford: Elsevier-Pergamon.

Sang H, Xia QL, Zhao J and Jiang Z (2015) Characteristic comparison of oxygen fugacity for ore fluids from Xiaolonghe and Lailishan greisen type Sn deposits in the west Yunnan province. *Contributions to Geology and Mineral Resources Research* **30**, 321–30 (in Chinese with English abstract).

Sawyer EW, Cesare B and Brown M (2011) When the continental crust melts. *Elements* **7**, 229–34.

Scaillet B, Holtz F and Pichavant M (2016) Experimental constraints on the formation of silicic magmas. *Elements* **12**, 109–14.

Shi YR, Wu ZH, Kröner A, Fan TY and Yang ZY (2015) Age and origin of Paleogene granitoids from Western Yunnan Province, China: geochemistry, SHRIMP zircon ages, and Hf-in-zircon isotopic compositions. *Acta Geologica Sinica (English Edition)* **89**, 1601–15.

Song SG, Niu YL, Wei CJ, Ji JQ and Su L (2010) Metamorphism, anatexis, zircon ages and tectonic evolution of the Gongshan block in the northern Indochina continent—an eastern extension of the Lhasa Block. *Lithos* **120**, 327–46.

Spencer CJ, Roberts NMW and Santosh M (2017) Growth, destruction, and preservation of Earth's continental crust. *Earth-Science Reviews* **172**, 87–106.

Stepanov A, Mavrogenes JA, Meffre S and Davidson P (2014) The key role of mica during igneous concentration of tantalum. *Contributions to Mineralogy and Petrology* **167**, 1009. doi: 10.1007/s00410-014-1009-3.

Streckeisen A and Le Maitre RW (1979) A chemical approximation to the modal QAPF classification of the igneous rocks. *Neues Jahrbuch fur Mineralogie, Abhandlungen* **136**, 169–206.

https://doi.org/10.1017/S0016756819001493 Published online by Cambridge University Press

Sun ZR, Dong GC, Zhao ZX, Wang WQ and Liu SQ (2017) Petrological, geochemical and geochronological features of Lailishan granitoids in western Yunnan and their genesis of partial melting of crustal source. *Geology in China* **44**, 1140–58 (in Chinese with English abstract).

Sun S-S and McDonough W (1989) Chemical and isotopic systematics of oceanic basalts: implications for mantle composition and processes. In *Magmatism in the Ocean Basins* (eds AD Saunders and MJ Norry), pp. 313–45. Geological Society of London, Special Publication no. 42.

Tang M, Lee CA, Chen K, Erdman M, Costin G and Jiang H (2019) Nb/Ta systematics in arc magma differentiation and the role of arclogites in continent formation. *Nature Communications* **10**, 235. doi: 10.1038/s41467-018-08198-3.

Tischendorf G (1977) Geochemical and petrographic characteristics of silicic magmatic rocks associated with rare element mineralization. In *Metallization Associated with Acid Magmatism, Vol. 2* (eds M Stemprok, L Burnol, G Tischendorf), pp. 41–96. Prague: Geological Survey of Czechoslovakia.

Wan X (2018) *Geochemistry and petrogenesis of Gudong and Menglian granite plutons in Tengchong Block, southeastern China*. M.Sc. thesis, University of Science and Technology of China, Hefei, China, 80 pp. (in Chinese with English abstract). Published thesis.

Wan X, Yang YZ, Li SQ and Chen FK (2018) Zircon U–Pb ages, geochemistry and Sr–Nd–Pb isotope characteristics of Menglian granites and their dark enclaves in Tengchong block of Western Yunnan, China. *Journal of Earth Sciences and Environment* **40**, 563–81 (in Chinese with English abstract).

Wang YJ, Li SB, Ma LY, Fan WM, Cai YF, Zhang YH and Zhang FF (2015) Geochronological and geochemical constraints on the petrogenesis of Early Eocene metagabbroic rocks in Nabang (SW Yunnan) and its implications on the Neotethyan slab subduction. *Gondwana Research* **27**, 1474–86.

Wang JY and Santosh M (2019) Eoarchean to Mesoarchean crustal evolution in the Dharwar craton, India: evidence from detrital zircon U–Pb and Hf isotopes. *Gondwana Research* **72**, 1–14.

Wang YJ, Zhang LM, Cawood PA, Ma LY, Fan WM, Zhang AM, Zhang YZ and Bi XW (2014) Eocene supra-subduction zone mafic magmatism in the Sibumasu Block of SW Yunnan: implications for Neotethyan subduction and India–Asia collision. *Lithos* **206–207**, 384–99.

Wu JD (2014) *The magmatic origin of Banggunjianshan and Polunshan granitoids in Tengchong Block, western Yunnan*. M.Sc. thesis, University of Science and Technology of China, Hefei, China, 73 pp. (in Chinese with English abstract). Published thesis.

Wu FY, Liu XC, Ji WQ, Wang JM and Yang L (2017) Highly fractionated granites: recognition and research. *Science China Earth Sciences* **60**, 1201–19.

Xie JC, Zhu DC, Dong GC, Zhao ZD, Wang Q and Mo XX (2016) Linking the Tengchong Terrane in SW Yunnan with the Lhasa Terrane in southern Tibet through magmatic correlation. *Gondwana Research* **39**, 217–29.

Xu YG, Lan JB, Yang QJ, Huang XL and Qiu HN (2008) Eocene break-off of the Neo-Tethyan slab as inferred from intraplate-type mafic dykes in the Gaoligong orogenic belt, eastern Tibet. *Chemical Geology* **255**, 439–53.

Xu ZQ, Wang Q, Cai ZH, Dong HW, Li HQ, Chen XJ, Duan XD, Cao H, Li J and Burg JP (2015) Kinematics of the Tengchong Terrane in SE Tibet from the late Eocene to early Miocene: insights from coeval mid-crustal detachments and strike-slip shear zones. *Tectonophysics* **665**, 125–48. doi: 10.1016/j.tecto.2015.09.033.

Xu YG, Yang QJ, Lan JB, Luo ZY, Huang XL, Shi YR and Xie LW (2012) Temporal–spatial distribution and tectonic implications of the batholiths in the Gaoligong–Tengliang–Yingjiang area, western Yunnan: constraints from zircon U–Pb ages and Hf isotopes. *Journal of Asian Earth Sciences* **53**, 151–75.

Yang ZY, Wang Q, Zhang CF, Dan W, Zhang XZ, Qi Y, Xia XP and Zhao ZH (2018) Rare earth element tetrad effect and negative Ce anomalies of the granite porphyries in southern Qiangtang Terrane central Tibet: new insights into the genesis of highly evolved granites. *Lithos* **312**, 258–73.

Yang JH, Wu FY, Wilde SA, Xie LW, Yang YH and Liu XM (2007) Tracing magma mixing in granite genesis: in situ U–Pb dating and Hf-isotope analysis of zircons. *Contributions to Mineralogy and Petrology* **153**, 177–90.

Yang QJ, Xu YG, Huang XL and Luo ZY (2006) Geochronology and geochemistry of granites in the Gaoligong tectonic belt, western Yunnan: tectonic implications. *Acta Petrologica Sinica* **22**, 817–34 (in Chinese with English abstract).

Yang QJ, Xu YG, Huang XL, Luo ZY and Shi YR (2009) Geochronology and geochemistry of granites in the Tengliang area, western Yunnan: tectonic implication. *Acta Petrologica Sinica* **25**, 1092–104 (in Chinese with English abstract).

Yang XC, Ye PS, Ye MN, Wang Z, Luzhou YF, Na FC and Chang PY (2017) Petrogenesis of an early Eocene gabbro–granite complex in Kachang (SW Yunnan) and its implications for Eocene magmatism in the Tengchong terrane of SW China. *International Geology Review* **60**, 825–43.

Yu L (2016) *Genesis and tectonic significance of the Mesozoic granitoids in the Tengchong-Baoshan Block, Sanjiang Area*. Ph.D. thesis, China University of Geosciences (Beijing), Beijing, China. 137 pp. Published thesis.

Yunnan BGMR (Yunnan Bureau Geological Mineral Resource) (1990) *Regional Geology of Yunnan Province*. Beijing: Geology Publication House, 729 pp. (in Chinese with English abstract)

Zhang Y, Jin CH, Fan WY, Zhang H, Shen ZW, Gao JH and Cheng WB (2013) Geochemical characteristics and classification of granites related to tin deposits in the Tengchong area, Southwest China. *Acta Geologica Sinica* **87**, 1853–63 (in Chinese with English abstract).

Zhang JY, Peng TP, Fan WM, Zhao GC, Dong XH, Gao JF, Peng BX, Wei C, Xia XP, Chen LL and Liang XR (2018) Petrogenesis of the Early Cretaceous granitoids and its mafic enclaves in the Northern Tengchong Terrane, southern margin of the Tibetan Plateau and its tectonic implications. *Lithos* **318–319**, 283–98.

Zhang QW, Wang QF, Li GJ and Cui XL (2018) Fractionation process of high-silica magmas through the lens of zircon crystallization: a case study from the Tengchong Block, SW China. *Chemical Geology* **496**, 34–42.

Zhang LX, Wang Q, Zhu DC, Li SM, Zhao ZD, Zhang LL, Chen Y, Liu SA, Zheng YC, Wang R and Liao ZL (2019) Generation of leucogranites via fractional crystallization: a case from the Late Triassic Luoza batholith in the Lhasa Terrane, southern Tibet. *Gondwana Research* **66**, 63–76.

Zhang W, Zhang ST, Cao HW, Wu JD, Xiao CX, Chen HJ and Tang L (2014) Characteristics of chlorite minerals from Xiaolonghe tin deposit in West Yunnan, China and their geological implications. *Journal of Chengdu University of Technology (Science & Technology Edition)* **41**, 318–28 (in Chinese with English abstract).

Zhao SW, Lai SC, Pei XZ, Qin JF, Zhu RZ, Tao N and Gao L (2019) Compositional variations of granitic rocks in continental margin arc: constraints from the petrogenesis of Eocene granitic rocks in the Tengchong Block, SW China. *Lithos* **326–327**, 125–43.

Zhao SW, Lai SC, Qin JF and Zhu RZ (2016a) Petrogenesis of Eocene granitoids and microgranular enclaves in the western Tengchong Block: constraints on eastward subduction of the Neo-Tethys. *Lithos* **264**, 96–107.

Zhao SW, Lai SC, Qin JF and Zhu RZ (2016b) Tectono-magmatic evolution of the Gaoligong belt, southeastern margin of the Tibetan plateau: constraints from granitic gneisses and granitoid intrusions. *Gondwana Research* **35**, 238–56.

Zhao SW, Lai SC, Qin JF, Zhu RZ and Gan BP (2017a) The petrogenesis and implications of the Early Eocene granites in Lianghe area, Tengchong Block. *Acta Petrologica Sinica* **33**, 191–203 (in Chinese with English abstract).

Zhao SW, Lai SC, Qin JF, Zhu RZ and Wang JB (2017b) Geochemical and geochronological characteristics of Late Cretaceous to Early Paleocene granitoids in the Tengchong Block, Southwestern China: implications for crustal anatexis and thickness variations along the eastern Neo-Tethys subduction zone. *Tectonophysics* **694**, 87–100.

Zhu RZ (2017) *Petrogenesis and geodynamic implications of Early Cretaceous granitic rocks in the Tengchong Block, SW China*. Ph.D. thesis, Northwest University, Xi'an, China, 259 pp. (in Chinese with English abstract). Published thesis.

Zhu RZ, Lai SC, Qin JF and Zhao SW (2015) Early-Cretaceous highly fractionated I-type granites from the northern Tengchong block, western Yunnan, SW China: petrogenesis and tectonic implications. *Journal of Asian Earth Sciences* **100**, 145–63.

Zhu RZ, Lai SC, Qin JF and Zhao SW (2018a) Early-Cretaceous syenites and granites in the northeastern Tengchong block, SW China: petrogenesis and tectonic implications. *Acta Geologica Sinica (English Edition)* **92**, 1349–65.

Zhu RZ, Lai SC, Qin JF and Zhao SW (2018b) Petrogenesis of late Paleozoic-to-early Mesozoic granitoids and metagabbroic rocks of the Tengchong Block, SW China: implications for the evolution of the eastern Paleo-Tethys. *International Journal of Earth Sciences* **107**, 431–57.

Zhu RZ, Lai SC, Qin JF, Zhao SW and Santosh M (2018c) Strongly peraluminous fractionated S-type granites in the Baoshan Block, SW China: implications for two-stage melting of fertile continental materials following the closure of Bangong-Nujiang Tethys. *Lithos* **316–317**, 178–98.

Zhu RZ, Lai SC, Qin JF, Zhao SW and Wang JB (2017a) Late Early-Cretaceous quartz diorite–granodiorite–monzogranite association from the Gaoligong belt, southeastern Tibet Plateau: chemical variations and geodynamic implications. *Lithos* **288–289**, 311–25.

Zhu RZ, Lai SC, Santosh M, Qin JF and Zhao SW (2017b) Early Cretaceous Na-rich granitoids and their enclaves in the Tengchong Block, SW China: magmatism in relation to subduction of the Bangong–Nujiang Tethys ocean. *Lithos* **286–287**, 175–90.

https://doi.org/10.1017/S0016756819001493 Published online by Cambridge University Press